Journal of Physics B: Atomic,
Molecular and Optical Physics

TOPICAL REVIEW

Macroscopic aspects of attosecond pulse generation

To cite this article: Mette B Gaarde *et al* 2008 *J. Phys. B: At. Mol. Opt. Phys.* **41** 132001

IOP PUBLISHING JOURNAL OF PHYSICS B: ATOMIC, MOLECULAR AND OPTICAL PHYSICS

J. Phys. B: At. Mol. Opt. Phys. **41** (2008) 132001 (26pp) doi:10.1088/0953-4075/41/13/132001

TOPICAL REVIEW

Macroscopic aspects of attosecond pulse generation

Mette B Gaarde, Jennifer L Tate and Kenneth J Schafer

Department of Physics and Astronomy, Louisiana State University, Baton Rouge, LA 70803-4001, USA

E-mail: gaarde@phys.lsu.edu

Received 16 April 2007, in final form 22 May 2008
Published 23 June 2008
Online at stacks.iop.org/JPhysB/41/132001

Abstract

Attosecond pulses are generated by a macroscopic number of ionizing atoms interacting with a focused laser pulse, via the process of high harmonic generation. The physics of their generation consists of an interplay between the microscopic laser–atom interaction and macroscopic effects due to ionization and phase matching in the nonlinear medium. In this review, we focus on a complete understanding of the way in which attosecond pulses arrive at a target where they can be characterized and used in an experiment. We discuss a number of results from calculations of attosecond pulse generation obtained by simultaneous solution of the time-dependent Schrödinger equation and the Maxwell wave equation. These results, which allow for a clean separation of microscopic and macroscopic factors, illustrate how macroscopic effects are used to select attosecond pulses from the radiation that is emitted by atoms interacting with a strong laser field.

1. Introduction

The production of sub-femtosecond pulses of extreme ultraviolet (XUV) radiation in recent years has allowed physical processes to be studied on the attosecond time scale for the first time [1–10]. Attosecond pulses (1 as $= 10^{-18}$ s) are now available in several laboratories as either single sub-femtosecond bursts or as trains of attosecond pulses. They are generated when a strong, infrared (IR) laser field rapidly ionizes a gas of atoms [11, 12]. Because the laser field interacts with a macroscopic number of atoms, the full description of this process requires solving not only the strong-field laser–atom interaction at the microscopic level, but also the Maxwell wave equation which describes, at the macroscopic level, the propagation of the radiation through the nonlinear medium. In this review, we focus on a complete understanding of the way in which attosecond pulses actually arrive at a target where they can be characterized and used in an experiment to study sub-femtosecond dynamics. Our goal is to broaden the understanding of attosecond pulse generation beyond the single-atom level, where one thinks about the emission in terms of the laser–atom interaction alone, to include macroscopic aspects of the process. The motivation for doing so is simple: as we will see, any process that produces attosecond pulses necessarily relies on a combination of microscopic and macroscopic effects, since single atoms alone, interacting with strong laser fields, do not emit pulses of attosecond radiation.

The process that leads to attosecond XUV emission begins at the single-atom level, when an electron in a spatially localized bound state encounters a linearly polarized laser field of sufficient strength to cause ionization. As the amplitude of the laser field rises and falls periodically, part of the bound state wavefunction evolves into a continuum wave packet, initially with very little energy. These wave packets, released every half cycle of the laser oscillation, can continue to interact with the ion core but they can also gain energy from the laser field [13]. Part of each wave packet will move away from the ion core never to return, but another part will be driven back towards the ion core, returning after about one optical cycle. When it reaches the vicinity of the core the wave packet can spatially overlap with the remaining bound-state amplitude, which leads to a time-dependent dipole moment and stimulated photon emission. This harmonic generation process, as it is called, converts some of the energy absorbed by the electron from the IR field into short-wavelength radiation in the XUV [14, 15]. The single-atom spectrum of radiation consists of a

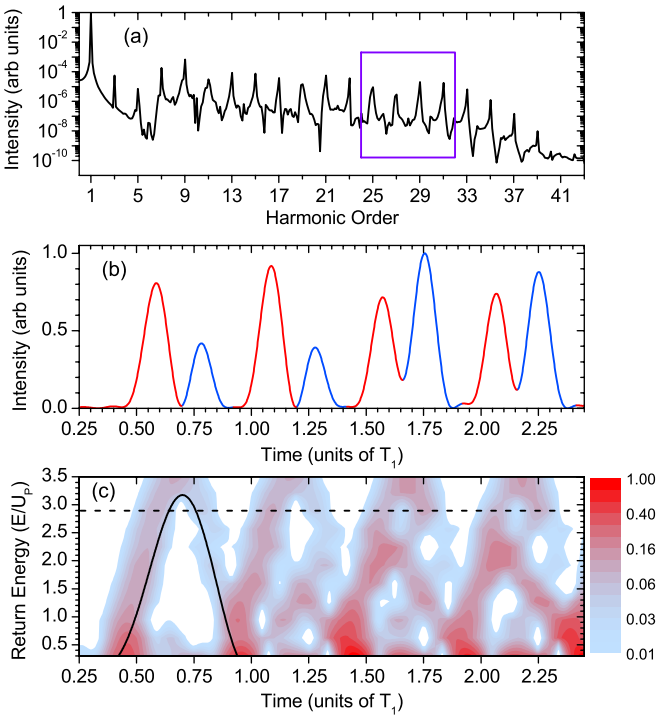

Figure 1. (a) The single-atom harmonic generation spectrum from an argon atom exposed to an 800 nm laser pulse. The flat top laser pulse has an intensity of 1.6×10^{14} W cm^{-2}, which gives rise to a cutoff energy around the 30th harmonic (46 eV). Odd harmonics are visible throughout the spectrum. (b) The time-dependent intensity (electric field squared) of the radiation obtained by selecting the boxed portion of the spectrum in part (a) and Fourier transforming to the time domain. The radiation consists of two trains of overlapping pulses, one each from the 'short' and 'long' quantum paths, which are shown in different shades for clarity. (c) The time history of the harmonic radiation shown in part (a) obtained via a time-frequency analysis of the full time-dependent dipole radiation, see [27] for details. The solid black line shows the semi-classical prediction for the return energy of the two shortest trajectories. The dotted horizontal line indicates the central frequency of the range of harmonics used to construct the pulse train shown in part (b). Parts (b) and (c) make clear that the harmonic peaks in the single-atom spectrum contain contributions from multiple quantum paths, leading to multiple attosecond bursts in each half cycle.

rapid decline for the low orders followed by a long plateau of constant strength, and a cutoff that depends on the wavelength and intensity of the driving laser [16], see figure 1(a). The harmonic spectrum can stretch from the infrared all the way to the soft x-ray region [17–19]. The radiation is emitted in a dipole pattern and has, in general, a very complex time structure that reflects the fact that the amplitude for emitting an XUV photon is the coherent sum over all of the different ways in which the emission can occur [20].

Although single atoms do not emit attosecond pulses when interacting with strong IR fields (see figure 1(c)), there is a natural attosecond time scale that characterizes the harmonic generation process. This can best be appreciated in the context of the semiclassical description of the quantum wave packet dynamics described in the previous paragraph [21]. In this picture, the amplitude for any strong-field process can be expressed as a coherent sum over only a few quantum orbits. These spacetime trajectories follow a sequence of release into the continuum (ionization), acceleration in the IR field, and return to the ion core, where photon emission takes place as the electron 'recombines' to the initial state. To a very good approximation, these quantum orbits can be described by the classical trajectory of an electron in an oscillating electric field, where the quantum phase is obtained from the classical action associated with a given trajectory. A specific electron trajectory begins at the ion core at a specified time, with zero initial velocity. This ionization time, and the laser intensity, then determine the possible times when an electron can return to the ion core and recombine, as well as the energy at the time of return. The emitted photon energy is simply the return energy plus the ionization potential (since the electron recombines).

In the semiclassical model of harmonic generation, the highest return energy that is possible defines the cutoff in the single-atom spectrum, and occurs at only one return time in each half cycle [22, 23]. For any energy below the cutoff there will be more than one quantum path, corresponding to different sets of ionization and return times, with the same return energy. Because the wave packet spreads rapidly in the continuum, it is usually the case that only the two quantum paths with travel times in the continuum of less than one optical cycle are important [24, 25]. The return energy for these two families of trajectories is a smooth function of the return time in each half cycle. The different quantum paths can be recognized in the time profile of a number of harmonics selected from the spectrum, see figure 1(b) and (c). Near the cutoff there is one burst per half cycle, while in the plateau region below the cutoff there are (at least) two bursts per half cycle. From this simple picture we see that although there is a natural attosecond time scale in that quantum paths with similar return energies also have similar return times [26], the unfiltered single-atom emission bears little resemblance to a useable attosecond pulse.

In fact, the XUV radiation signal generated in a strong field laser–matter interaction experiment and measured at a target downstream is not the dipole radiation pattern from a single atom. Rather, it is the spectral intensity (and sometimes phase) distribution of the XUV electric field at the target. This electric field is the coherent sum of the radiation from all the atoms in the gas and is a result of constructive interference mostly in the forward direction. The constructive interference is commonly referred to as 'phase matching' of the radiation since it relies on matching the phase front of newly generated radiation at one point in the gas to the phase front of the field that is already propagating at the same frequency. A full description of the XUV radiation that arrives at a target must therefore account for the single-atom emission, macroscopic propagation, and any filtering of the radiation after the medium and before the target.

In this paper, we review a number of results from 'complete' calculations of attosecond pulse generation schemes obtained by simultaneous solution of the time-dependent Schrödinger equation (TDSE) to describe the microscopic laser–atom interaction and the Maxwell wave equation (MWE) to describe the macroscopic propagation and

phase matching of the radiation. The theoretical methods have been well validated by comparison to a number of experiments as described in the references throughout, however, we will not spend much time comparing to experiments explicitly. This is because our focus is on the interaction between the microscopic and macroscopic aspects of attosecond pulse generation, and a separation of these factors is possible only within a theoretical framework since experiments always measure an outcome that convolutes these factors. For further discussions of experimental results we refer the reader to [11, 12].

A key result obtained from the calculations we will describe is that it is never the case that attosecond pulses are 'generated' *per se*, but rather that they are 'selected'. The difference is crucial, since one view leads to a simplistic focus on single-atom dynamics, whereas the other leads to an appreciation of how various microscopic and macroscopic processes interact to produce an attosecond pulse on a target. To produce a usable attosecond pulse the enormous XUV radiation spectrum that results from the strong-field laser–atom interaction must be gated and/or filtered, most often in time, space and frequency. That is, we look for natural groupings of radiation, in frequency, space and time, that can give isolated attosecond pulses (if the driving laser pulse is only a few IR cycles in duration) or trains of distinct attosecond pulses (if the driving pulse is longer). Macroscopic effects always play a role in this process, sometimes enabling the process and sometimes inhibiting it. To understand how attosecond pulses can be either optimized or even produced via new methods, as will certainly be necessary for attosecond science to progress, it is important to understand the various filtering and gating schemes that are employed (sometimes without complete knowledge of them). More generally, we feel certain that thinking of attosecond pulse generation only in terms of the single-atom dynamics not only limits the imagination, it also disregards potentially useful nonlinearities at the macroscopic level which could be used to produce shorter, more intense pulses.

In the following section, we begin our examination of the macroscopic aspects of attosecond pulse generation with a review of phase matching as it applies to strong field XUV generation. Much of the material applies to harmonic generation in general, since present-day attosecond pulses are, as we said, selected from the radiation produced in a typical harmonic generation experiment. These experiments employ focused, 800 nm laser pulses interacting with atomic gas media. The driving pulses last from 5–50 fs and typically have peak intensities between 10^{14} W cm^{-2} and 10^{15} W cm^{-2}. In addition to discussing the phase matching of the harmonics, we examine factors like ionization and other dispersive effects that can reshape the driving pulse and impact the XUV radiation that is produced. We next give a detailed account of the theoretical methods that are used to simultaneously solve the TDSE and the MWE, including the strong-field approximation (SFA) for solving the TDSE and the slowly evolving wave approximation for the MWE.

Following this theoretical preface, we begin by discussing the role that phase matching plays as a temporal gate in the production of attosecond pulse trains [2, 26]. The temporal gating can happen in the nonlinear medium, when one family of trajectories is preferably produced, or after the medium via the spatial separation of the different trajectories. Spectral filtering is also necessary in this case, as only a range of plateau harmonics can yield short pulses. We then discuss the production of isolated or single attosecond pulses (SAPs). The most straightforward methods use 5 fs driving laser pulses with a well-controlled carrier envelope phase as a time gate on the emission of a range of frequencies, combined with spectral filtering. One method uses a single few-cycle driving pulse to time gate the emission near the high harmonic cutoff [4, 5, 28–32], while another uses two such pulses with orthogonal polarizations to create a time gate in the emission of plateau harmonics [33–41]. In both cases macroscopic effects can inhibit or, perhaps surprisingly, enable the production of isolated pulses. The use of few-cycle IR pulses to drive isolated attosecond pulse production makes these schemes technically very demanding and there is wide interest in using longer driving pulses to produce SAPs. We review two methods for this, ionization-induced reshaping of the driving laser pulse, which allows a far-field spectral and spatial filter to act as a time gate, and phase-matching used as a spatio-temporal gate [42, 43].

We end our review by discussing novel methods for producing attosecond pulses. These include using longer wavelength driving lasers (in the mid-infrared) [11, 27, 44–49] and using two-colour driving fields with one of the colours being the familiar 800 nm used in most experiments to date [50–52]. Two-colour methods offer increased control over attosecond pulse generation, allowing for the tailoring of attosecond pulse trains, as well as allowing for using longer driving pulses. The key challenge, as we show, is to keep all of the control parameters roughly constant over the interaction region, something that is made difficult by macroscopic effects. We end by briefly reviewing what we see as the biggest challenges for attosecond pulse generation over the next few years.

2. Phase matching

The XUV electric field generated and measured in a strong field laser–matter interaction experiment results from the coherent sum of the radiation from all the atoms in the nonlinear medium, which interferes constructively mostly in the forward direction. By constructive interference we mean that the radiation generated at a position z_2 some distance into the nonlinear medium must be in phase with the radiation that was generated at an earlier position $z_1 < z_2$ and then propagated to position z_2. In the most general terms, phase matching is the matching of the phase front of the newly generated field to the phase front of the propagating field, which mathematically can be expressed as

$$\vec{k}_{\text{source}} = \vec{k}_{\omega}, \tag{1}$$

where $\vec{k}_{\omega}$ is the wave vector of the propagating field with angular frequency ω and $\vec{k}_{\text{source}}$ is the wave vector of the newly generated field which depends on the phase variation

of the source term (the nonlinear polarization field), $\vec{k}_{\text{source}} = \vec{\nabla}\phi_{\text{source}}(r, z)$.

The generation of attosecond pulses, and more generally of high-order harmonics, is a highly nonlinear process which is the result of an intense, focused laser beam interacting with and propagating through a macroscopic number of ionizing atoms. There are a number of effects that influence the phase variation of the source term and therefore the phase matching and build-up of the harmonic radiation. We discuss the most important ones next.

2.1. Phase matching in the absence of ionization and other dispersive effects

There is a range of experimental conditions for generating high harmonics and attosecond pulses where one can think of phase matching without considering effects of ionization. These include when the laser intensity is safely below saturation and the ionization rate is not rapidly changing in time, when the atomic density is low (few tens of Torr pressure), and the medium is short compared to the length over which ionization-induced defocusing and dephasing occur. The two biggest contributions to the phase variation of the source term are then the geometrical phase variation $\phi_{\text{focus}}(r, z)$ due to the focused laser beam, and the intrinsic intensity-dependent phase $\phi_{\text{dip},j}(r, z)$ of the dipole radiation which we will describe in more detail below [24, 53–55]. In such conditions, we can write the phase matching requirement as

$$\vec{k}_{\text{dip},j}(r, z) + \frac{\omega}{\omega_1}(\vec{k}_{\text{focus}}(r, z) + \vec{k}_1) = \vec{k}_\omega, \tag{2}$$

or

$$\vec{\nabla}\phi_{\text{dip},j}(r, z) + \frac{\omega}{\omega_1}\vec{\nabla}\phi_{\text{focus}}(r, z) + \frac{\omega}{c}\vec{e}_z = \vec{k}_\omega, \tag{3}$$

where ω_1 and $\vec{k}_1$ are the central frequency and wave vector of the laser light, $\vec{e}_z$ is a unit vector in the propagation direction, and we have used cylindrical coordinates. In writing equation (3) we have also ignored effects of linear dispersion of the gas medium, i.e. we assume that the refractive index is equal to one for both the laser and the XUV fields. Balcou and collaborators suggested that the degree of phase matching according to equation (3) can be represented via the phase mismatch $\Delta k_\omega(r, z)$ given by [55]

$$\Delta k_\omega(r, z) = \frac{\omega}{c} - \left|\vec{k}_{\text{dip},j}(r, z) + \frac{\omega}{\omega_1}(\vec{k}_{\text{focus}}(r, z) + \vec{k}_1)\right|. \tag{4}$$

This corresponds to requiring that the length of the wave vector of the propagating XUV field, which is chosen to be ω/c, should equal the length of the wave vector of the newly generated XUV field which has had the dipole and the focusing phase imposed on it. Equation (4) implicitly assumes that the XUV field predominantly propagates in the forward direction.

For a Gaussian beam, the phase variation of the laser beam due to focusing is given by

$$\phi_{\text{focus}}(r, z) = -\tan^{-1}\left(\frac{2z}{b}\right) + \frac{2k_1 r^2 z}{b^2 + 4z^2}, \tag{5}$$

where b is the confocal parameter of the beam [56]. On axis ($r = 0$), the phase from focusing (the Gouy phase) decreases monotonically from $\pi/2$ to $-\pi/2$. This gives a negative contribution to the wave vector of the laser field and causes the laser wave fronts to advance faster than they would in the absence of focusing.

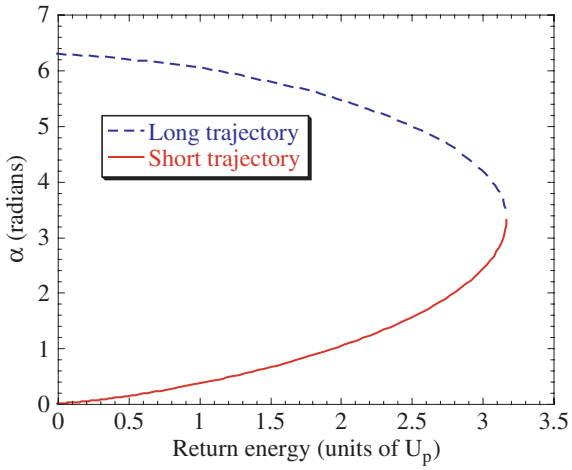

Figure 2. The phase coefficient α calculated as the action integral over the two shortest electron trajectories in the semi-classical model is plotted as a function of electron return energy, in units of U_p.

The spatial variation of the dipole phase $\phi_{\text{dip},j}(r, z)$, through its dependence on the laser field intensity, has important consequences for phase matching and for the temporal and spatial coherence properties of the XUV radiation [53, 57–59]. The intensity dependence of the dipole phase can be understood from the semi-classical model [24, 53, 59]. The phase of the time-dependent dipole moment is the phase accumulated by the electron wave packet during its acceleration by the laser field between time of release t' and time of return t and is given by the action integral

$$\phi(t', t) = -\int_{t'}^{t} S(t'')\,\mathrm{d}t'', \tag{6}$$

where $S(t'') = E_{\text{kin}}(t'') - E_{\text{pot}}(t'')$ is the classical action given by the difference between the kinetic and the potential energy. In the long-pulse limit, the kinetic energy of the electron is proportional to the ponderomotive energy of the driving field (and thereby the intensity I, since $U_p \propto I/\omega_1^2$), with a proportionality constant α that depends on the time spent in the continuum. For a given electron trajectory j defined by a specific time of release and return and thereby a specific return energy ω, we write the phase as $-\alpha_j U_p/\omega_1$ (in atomic units). The phase constant increases monotonically with the time spent in the continuum. A plot of α_j as a function of return energy for the two shortest electron trajectories is shown in figure 2, calculated for a monochromatic field as outlined in equations (15)–(16) of [21].

Figure 2 shows that for each XUV energy in the plateau region, the different quantum path contributions to the dipole moment have different intensity-dependent phases, each with a phase coefficient that changes with XUV energy. For a range of energies in the plateau region α_1 (for the short trajectory) is small and α_2 (long trajectory) is large, and for energies closer to the cutoff region the two phase coefficients become

more similar. We note here that even though the dipole phase is strictly proportional to the intensity only in the long-pulse limit, writing the phase variation as $\phi_{\mathrm{dip},j} = -\alpha_j U_\mathrm{p}/\omega_1$ is a very good approximation even for pulses as short as three optical cycles [60].

The *spatial* variation of the focused laser beam intensity means that the conditions for good phase matching in general are very different for the two quantum path contributions to a given XUV energy, and that the phase matching conditions also vary with XUV energy [61, 62]. As a simple example, let us consider the phase matching condition from equation (4) along the axis of propagation only, for one quantum path contribution j,

$$\Delta k_\omega(z) = \alpha_j \frac{\mathrm{d}\,(U_\mathrm{p}/\omega_1)}{\mathrm{d}z} + \frac{\omega}{\omega_1}\frac{2}{b(1+(2z/b)^2)}. \qquad (7)$$

The second term in this equation is always positive so to achieve perfect phase matching on axis, we find the familiar result that we must place the nonlinear medium after the laser focus ($z = 0$) where the intensity is decreasing with z, so that $\mathrm{d}U_\mathrm{p}/\mathrm{d}z$ is negative.

Including the radial variation of the laser intensity and phase makes the phase matching conditions more complicated. Following Balcou and collaborators [55], the degree of phase matching from equation (4) can be represented graphically via the coherence length $L_\mathrm{coh}(r, z) = 2\pi/\Delta k_\omega(r, z)$ over which the XUV radiation can be expected to phase match constructively. Figure 3 shows an example of this representation, from Chipperfield and collaborators [63] who have calculated coherence lengths for different harmonics in neon generated by a 750 nm laser field with a peak intensity of approximately 4×10^{14} W cm^{-2} and a confocal parameter of 7 mm, see [63] for details. The phase matching conditions for the two quantum path contributions to the dipole moment are shown separately. A long (short) coherence length, corresponding to good (bad) phase matching, is shown with light (dark) colours in the figure.

The three harmonics shown in figure 3 span the plateau range in neon for the intensity used in the calculation. The 21st harmonic is in the lower plateau, the 35th harmonic in the middle and the 45th harmonic is close to the cutoff energy. It is clear from the figure that phase matching depends strongly on the phase coefficient α_j. For a given XUV energy (given harmonic) there is a big difference between the phase matching of the short and the long quantum path contribution. In general, it is easier to achieve reasonably good phase matching for the short path than for the long-path contributions. Because of the large intensity-dependent phase associated with the long trajectory contribution, its phase matching is much more specific to the focusing conditions, and its coherence length in the absence of perfect phase matching is very short. In contrast, the coherence length for the short trajectory contribution is more than 0.5 mm over most of the focus for the lowest harmonics. It is also interesting to note that for the case shown in the figure, a thin medium placed at a position of $z = 2$ mm will lead to almost identical degrees of phase matching for the short trajectory contribution to all three of the harmonics shown in the figure, which covers most of the plateau range of the harmonic spectrum. However, the figure

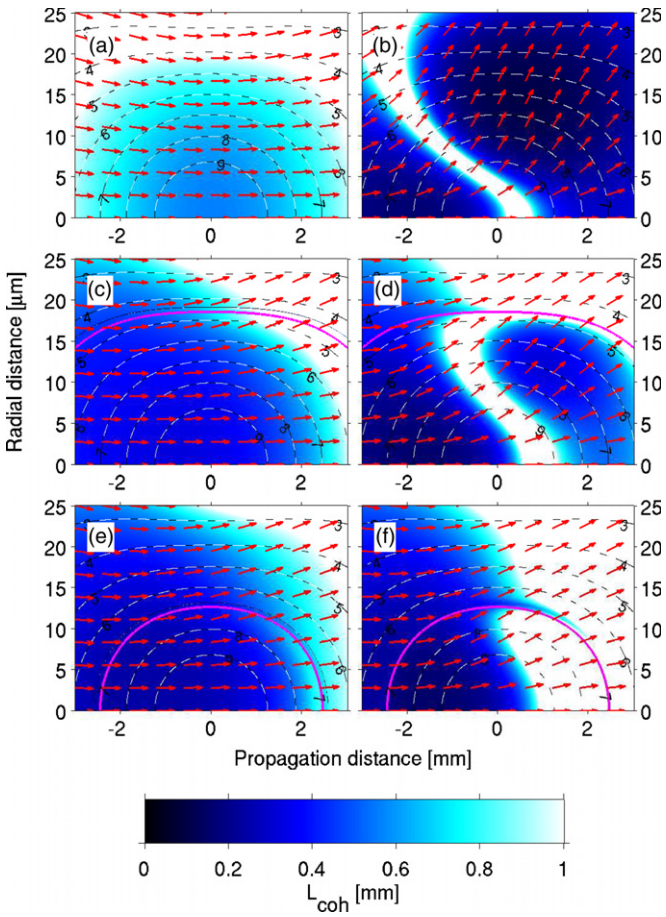

Figure 3. Phase matching maps for the two different quantum path contributions to the 21st (a–b), 35th (c–d) and 45th (e–f) harmonic in neon, driven by a 750 nm, 4×10^{14} W cm^{-2} laser pulse with a confocal parameter of 7 mm. The phase matching of the short (long)-path contribution to each harmonic is shown on the left (right). The (red) arrows in the figure indicate the direction of the wave vector $\vec{k}_\mathrm{source}$, which is the most likely direction of propagation for the XUV radiation. The solid (purple) lines mark the transition between the plateau and the cutoff region for each harmonic, see [63] for details. Reprinted from [63] with permission from Elsevier.

also shows that it is possible to obtain very good on-axis (or off-axis) phase matching for the long trajectory contribution to a small range of XUV energies over a short distance. For example, a thin nonlinear medium placed 0.5 mm after the focus will give rise to very good on-axis phase matching for the long trajectory contribution to the 21st harmonic.

2.2. Ionization-induced dispersion and non-adiabatic self-phase matching

In experimental configurations with high intensity or very short driving pulses, or high pressure or long media, it is no longer justified to ignore the effects of ionization on the propagation of the laser field and the phase matching of the generated XUV radiation. Examples of such configurations would be the generation of extremely high photon energies as in [18, 19, 44, 64], often using few-cycle driving pulses, or very long nonlinear media such as gas cells or wave guides

[18, 65, 66, 67]. Dispersion and absorption from neutral atoms can also play an important role in long media [67, 68, 69].

The presence of free electrons in the nonlinear medium resulting from the unavoidable laser-driven ionization changes the propagation dynamics of the laser field. The free electron contribution to the refractive index is negative, and is proportional to the free electron density and the wavelength squared [70]. In the spatial domain, this causes the laser phase front to advance faster on axis than off axis (since the intensity and thereby the electron density is highest on axis), which leads to defocusing of the beam. In the time domain, the increasing free electron density causes a (dynamical) blue shift of the driving laser frequency [70, 71]. These spatio-temporal propagation dynamics and their consequences for phase matching cannot be simply described in an adiabatic equation for the phase mismatch as in equation (4). However, we can estimate the dispersive effects of ionization and neutral atoms over a short distance where the free electron density is constant by expanding the on-axis phase mismatch equation (7) to include dispersion,

$$\Delta k_\omega(z) = \frac{\omega}{c}\Delta n_{at}(\omega) + \frac{\omega}{c}\Delta n_{\mathrm{el}}(\omega) + \alpha_j \frac{\mathrm{d}U_\mathrm{p}/\omega_1}{\mathrm{d}z} + \frac{\omega}{\omega_1}\frac{2}{b(1+(2z/b)^2)}, \tag{8}$$

where the difference in refractive index $\Delta n(\omega) = n(\omega) - n(\omega_1)$ is negative for the atomic contribution and positive for the free electron contribution. $\Delta n(\omega)$ also depends on z through the densities of neutral atoms and electrons.

At high intensity and high photon energies, the positive free electron contribution strongly dominates the neutral atom contribution, see for instance [54, 72]. Also for very high photon energies the positive focusing contribution to the phase mismatch, which scales with ω, strongly dominates the dipole contribution, which varies only slowly with ω over any limited range of the harmonic spectrum (see figure 2). The total phase mismatch is therefore positive which means that the phase fronts of the driving field, and thereby the source term, advance faster than the newly generated XUV field. In the adiabatic limit, this would make phase matching of very high-order harmonics (several hundred eV photon energies) very difficult and strongly limit their production efficiency.

Geissler and collaborators have shown that phase matching of these very high harmonics is much improved when using a few-cycle driving pulse [72]. In this case, there is a non-adiabatic contribution to the phase mismatch which is negative, and perfect phase matching can therefore be achieved for a large range of XUV energies over a short distance. The non-adiabatic phase mismatch is due to the ionization-induced blue shift which causes the laser frequency to increase with propagation distance (until ionization-induced defocusing reduces the intensity, at which point the laser frequency no longer changes). The shortening of the wavelength with z acts to slow down the advance of the driving field phase front and allows the XUV phase fronts to catch up. See [72] for a more detailed discussion of this mechanism which has been termed non-adiabatic self-phase matching (NSPM). In a recent experiment by Seres and collaborators the relatively efficient production of keV XUV energies was attributed to NSPM [19].

As a conclusion to this section on phase matching, let us note that although it is very useful and sometimes sufficient to think about the generation and phase matching of attosecond pulses in terms of adiabatic phase matching diagrams, the propagation of the laser field and the build-up of coherent XUV radiation in the macroscopic, ionizing medium is a process which is highly dynamical in both the temporal and spatial domain. Even the non-adiabatic self-phase matching mechanism described above does not take into account the spatial modulations of the laser field caused by ionization-induced defocusing. In the following section, we outline a theoretical approach to describing these large-scale extremely nonlinear dynamics and the XUV radiation that results from them.

3. Theoretical method

To calculate the XUV radiation generated in a macroscopic medium by an intense, focused laser pulse we numerically integrate the coupled, non-adiabatic solutions to the Maxwell wave equation (MWE) and the time-dependent Schrödinger equation (TDSE). This means that our description of the intense-laser–matter interaction includes both the response of a single atom to the laser pulse and the collective response of the macroscopic gas medium.

3.1. Propagation equations

We start from the MWE with source terms, written in the time domain as (using SI units)

$$\nabla^2 E(t) - \frac{1}{c^2}\frac{\partial^2}{\partial t^2}E(t) = \frac{1}{\epsilon_0 c^2}\frac{\partial^2}{\partial t^2}P(t). \tag{9}$$

where $E(t)$ is the time-dependent electric field of the driving and/or generated fields and $P(t)$ is the time-dependent polarization field representing for the moment all source terms for the driving and the generated field. Both $E(t)$ and $P(t)$ are functions of the cylindrical coordinates r and z. In a coordinate system that moves at the group velocity v_g of the pulse, $z' = z, t' = t - z/v_\mathrm{g}$, and after applying the slowly evolving wave approximation (SEWA, see [73] for details) the propagation equation becomes

$$\nabla_\perp^2 E(t') - \frac{2}{v_\mathrm{g}}\frac{\partial^2}{\partial z'\partial t'}E(t') + \left(\frac{1}{v_\mathrm{g}^2} - \frac{1}{c^2}\right)\frac{\partial^2}{\partial t'^2}E(t') = \frac{1}{\epsilon_0 c^2}\frac{\partial^2}{\partial t'^2}P(t'). \tag{10}$$

In contrast with the slowly varying envelope approximation, which also leads to a first-order propagation equation in z', the SEWA is valid for light pulses with durations as short as one optical cycle, as long as the amplitude and phase of the electric field are slowly varying (on the scale of the wavelength) in the propagation direction. The SEWA implies that we neglect backwards propagating waves, and is usually valid for the relatively dilute gases and moderate ionization rates we are considering in harmonic generation scenarios (see [73] for details). For an example of a Maxwell–Schrödinger equation solver that is not based on the SEWA but integrates

the full vectorial Maxwell equations, coupled to 3D numerical integrations of the time-dependent Schrödinger equation for molecules, see the work by Lorin and collaborators [74].

The SEWA propagation equation in equation (10) can be integrated directly in the time and space domain, as is done in [43, 73]. We follow the approach of Priori *et al* [75] and Shon *et al* [76] among others, and solve the propagation equation in the frequency domain after Fourier transforming with respect to t',

$$\nabla_\perp^2 \tilde{E}(\omega) + \frac{2\mathrm{i}\omega}{v_\mathrm{g}} \frac{\partial \tilde{E}(\omega)}{\partial z'} + \left[\frac{\omega^2}{c^2} - \frac{\omega^2}{v_\mathrm{g}^2} \right] \tilde{E}(\omega) = -\frac{\omega^2}{\epsilon_0 c^2} \tilde{P}(\omega). \tag{11}$$

The source term on the right-hand side describes the response of the medium to the electric field and includes both linear and nonlinear terms. It is often useful to separate the polarization field into its linear and nonlinear components $\tilde{P}(\omega) = \tilde{\chi}(\omega)\tilde{E}(\omega) + \tilde{P}_{NL}(\omega)$, where the linear susceptibility $\tilde{\chi}(\omega)$ includes both linear dispersion and absorption through its real and imaginary parts. This finally yields

$$\nabla_\perp^2 \tilde{E}(\omega) + \frac{2\mathrm{i}\omega}{v_\mathrm{g}} \frac{\partial \tilde{E}(\omega)}{\partial z'} + \left[\frac{\tilde{n}^2(\omega)\omega^2}{c^2} - \frac{\omega^2}{v_\mathrm{g}^2} \right] \tilde{E}(\omega) = -\frac{\omega^2}{\epsilon_0 c^2} \tilde{P}_{NL}(\omega), \tag{12}$$

where $\tilde{n}^2(\omega)$ is given by $1 + \tilde{\chi}(\omega)/\epsilon_0$. The nonlinear polarization field includes the effects of ionization and the generation of new frequencies via harmonic generation and is calculated in the time-domain via solution of the time-dependent Schrödinger equation in the strong field approximation, as described in more detail below. The linear response of the medium is included directly in the frequency domain via tabulated frequency-dependent values of dispersion and absorption coefficients. It is of course an approximation to split the polarization field into linear and nonlinear components. In particular, it is an approximation to write the linear response as a product of a frequency-dependent susceptibility and the Fourier components of the electric field, since in a rapidly ionizing medium even the linear response would be the Fourier transform of the product of the time-dependent density and the time-dependent atomic response. However, we are not dealing with situations where linear dispersion/absorption is dominating the dynamics, and it is therefore practical to divide the polarization field into its linear and nonlinear components, which allows us an easy way to include absorption of the high frequencies via one-photon ionization.

We next perform the very good approximation of not allowing the weak radiation generated via the nonlinear interactions to influence the strong driving electric field. In practice, this means that we separately solve propagation equations for the driving field $\tilde{E}_1(\omega)$ and the generated fields $\tilde{E}_h(\omega)$. For the driving field we ignore all linear dispersion and absorption effects which is justified due to the short propagation lengths (few millimetres) and moderate pressures (10–100 Torr) we are considering. For the generated fields we include absorption effects through frequency-dependent absorption coefficients $\tilde{\alpha}(\omega)$ obtained from [77]. The absorption coefficient is proportional to the density of neutral atoms. In the calculations shown in this paper we have not included linear dispersion due to neutral atoms, but it can be included using the frequency-dependent dispersion coefficients calculated in [78]. We thus have the two separate sets of equations (now dropping primes on the z-coordinate),

$$\nabla_\perp^2 \tilde{E}_1(\omega) + \frac{2\mathrm{i}\omega}{c} \frac{\partial \tilde{E}_1(\omega)}{\partial z} = -\frac{\omega^2}{\epsilon_0 c^2} \tilde{P}_\mathrm{ion}(\omega) \tag{13}$$

$$\nabla_\perp^2 \tilde{E}_h(\omega) + \frac{2\mathrm{i}\omega}{c} \frac{\partial \tilde{E}_h(\omega)}{\partial z} + \frac{\mathrm{i}\omega}{c} \tilde{\alpha}(\omega) \tilde{E}_h(\omega) = -\frac{\omega^2}{\epsilon_0 c^2} \tilde{P}_\mathrm{dip}(\omega). \tag{14}$$

In these equations we have specified that the source terms for the driving field, $\tilde{P}_\mathrm{ion}(\omega)$, and for the generated fields, $\tilde{P}_\mathrm{dip}(\omega)$, are different as described in more detail below.

We solve equations (13) and (14) for the driving field $\tilde{E}_1(\omega)$ and the generated fields $\tilde{E}_h(\omega)$ by space-marching through the ionizing nonlinear medium, using a Crank–Nicholson scheme. At each plane in the propagation direction z, we calculate the time-dependent driving field $E_1(t)$ as the Fourier transform of $\tilde{E}_1(\omega)$. We then calculate the nonlinear atomic response in the time-domain by solving the TDSE using $E_1(t)$ as the driving field (see below). The time-dependent atomic response is used to calculate the frequency-dependent source terms in the wave equation, which are then used for marching to the next plane in z.

3.2. Calculation of source terms

3.2.1. Source terms for the driving field. The source term $\tilde{P}_\mathrm{ion}(\omega)$ for the propagation of the driving laser field is due to the ionization of the medium, and is calculated from the time-dependent current density $J(t) = \frac{\partial P_\mathrm{ion}(t)}{\partial t}$ so that $-\frac{\omega^2}{\epsilon_0 c^2} \tilde{P}_\mathrm{ion}(\omega) = \widetilde{FT}\left[\frac{1}{\epsilon_0 c^2} \frac{\partial J(t)}{\partial t}\right]$, where $\widetilde{FT}$ denotes a Fourier transform. We follow the approach in [79] and include two contributions to the current density

$$\frac{\partial J_p(t)}{\partial t} = \frac{\mathrm{e}^2 N_e(t)}{m_e} E_1(t) \tag{15}$$

$$\frac{\partial J_\mathrm{abs}(t)}{\partial t} = \frac{\partial}{\partial t} \frac{\gamma(t) N_e(t) I_\mathrm{p} E_1(t)}{|E_1(t)|^2}, \tag{16}$$

where e and m_e are the electron charge and mass, $N_e(t)$ is the free electron density, $\gamma(t)$ is the ionization rate and I_p is the atomic ionization potential. The absorption term $J_\mathrm{abs}(t)$ describes the loss of energy from the laser field due to the ionization of the medium. This term is in general small in the conditions that are of interest for harmonic generation and production of attosecond pulses.

The plasma oscillation term $J_p(t)$ is due to the oscillatory motion of the free electrons in the laser electric field. It gives rise to a spatial and temporal variation of the refractive index, which in turn causes defocusing and self-phase modulation and gives rise to an additional phase mismatch in the propagation of the harmonics relative to the driving field. As we discussed in section 2, this term can be very important for how the

spatio-temporal shape of the laser electric field evolves during propagation through the nonlinear medium, especially in situations where the laser intensity and/or the atomic density is high, or when the driving pulse is very short.

How accurately one needs to calculate the time-dependent ionization probability depends on the generation configuration. There are a range of attosecond pulse generation scenarios where ionization is only of minor importance, for instance when the intensity and atomic density are relatively low, or when the medium is short compared to the laser confocal parameter. However, it is also important to keep in mind that harmonic generation is an ionization driven process—the first step in the semi-classical description of HHG is the tunnel ionization of the electron into the continuum—and that ionized electrons will always be around in a harmonic generation experiment. In situations where ionization plays a big role in the propagation dynamics of the laser pulse, an incorrect description of ionization quickly leads to substantially incorrect results.

In general, the consequence of overestimating ionization is that saturation happens at too low intensity, and too early in the medium along the propagation direction. In time it leads to a blue-shift which is too large and which remains with the driving pulse through the remainder of the medium. Underestimating or neglecting ionization leads to a too optimistic picture of the effective peak intensity driving the harmonic generation. To describe the short-pulse ionization dynamics correctly it is therefore crucial to accurately calculate $N_e(t)$ and $\gamma(t)$ with sub-cycle precision. Our calculation of $N_e(t)$ and $\gamma(t)$ originates in a numerical solution of the TDSE within the single active electron approximation [20] as described in more detail below.

In figure 4 we show a particular example of the importance of ionization in the propagation dynamics, calculating the evolution of the on-axis energy density of a laser field as it propagates through neon at a pressure of 150 Torr. We compare calculations where we have used ionization probabilities calculated via the widely used instantaneous ionization rates as proposed by Ammosov, Delone and Krainov (ADK) [80], and ionization probabilities corrected to better agree with a numerical integration of the TDSE in the single active electron approximation (SAE) [20]. The un-corrected ADK rates give rise to a 45% ionization probability at the beginning of the medium (compared with 15% for the corrected result), which leads to very fast defocusing of the beam. After about 1 mm of propagation, the intensity has been reduced by 35% and the radial profile has become very broad and flat (not shown in the figure). We also compare the resulting harmonic spectra at the end of the neon gas and show that the ADK-based calculation leads to a much lower cutoff energy.

In the following, we describe two different approaches to correcting the ADK results so they agree better with the SAE-TDSE result, without having to implement a direct numerical integration of the SAE-TDSE into the solution of the propagation equation. In the simplest correction scheme, we scale the intensity-dependent ADK rates $\gamma_{\mathrm{ADK}}(I_0)$ obtained as a function of the (constant) intensity I_0 with an intensity-dependent correction factor so that they agree better with

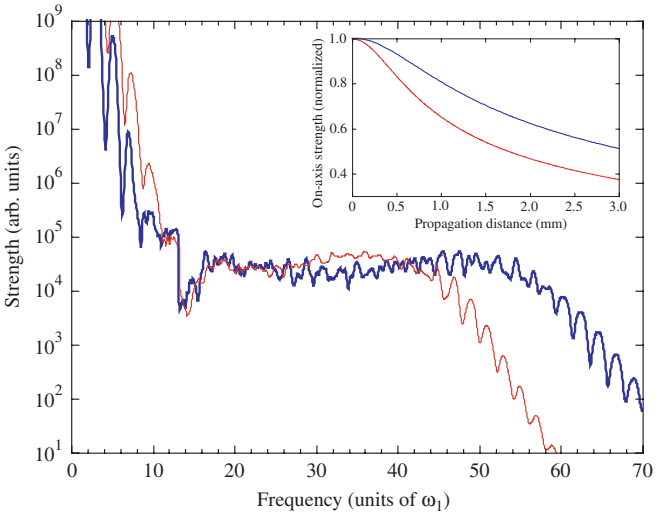

Figure 4. Difference in propagation dynamics caused by using ionization probabilities calculated in different ways. Thick (blue) lines are the result of using TDSE-corrected ADK rates, thin (red) lines are the result of using uncorrected ADK rates. In the inset we show the evolution of the on-axis energy density with propagation distance through a 3 mm long neon gas at a pressure of 150 Torr for a 750 nm, 7 fs driving pulse with an initial peak intensity of 9×10^{14} W cm^{-2}, in the figure itself we show the resulting radially integrated harmonic spectra at the end of the neon gas.

tabulated intensity-dependent TDSE ionization rates. We then carefully compare the time-dependent ionization probabilities that result from using the corrected ADK rates or the SAE rates, to make sure that the agreement is good over a range of peak intensities and pulse durations (we have typically used 1–3 $\times$ 10^{14} W cm^{-2} and pulse durations of 5–10 optical cycles, and so far only applied this in argon). This approach is adiabatic in nature since it relies on intensity-dependent ionization rates and implicitly assumes that the driving pulse is long.

For short driving pulses, where we are interested in the dynamical effects of a rapidly ionizing nonlinear medium, we have implemented a more elaborate correction of the *time-dependent* ADK ionization probability. We start by defining the time-dependent ionization probability in the TDSE calculation as the probability density of the wavefunction outside of a small volume around the ion core, $P_{\mathrm{vol}}(t)$. In figure 5(a) and (b) we show $P_{\mathrm{vol}}(t)$ for three different volumes, resulting from two different few-cycle driving pulses [81]. We also show the time-dependent ground-state population for comparison. The oscillations in the ionization probability calculated for the larger volumes result from the driven motion of the electron in the laser field, indicating that the electron at these radii can already be considered to be free and contributing to the plasma oscillation. We therefore use the smallest radius (10 au) to define $P_{\mathrm{vol}}(t)$. Next, we compare $P_{\mathrm{vol}}(t)$ to $P_{\mathrm{ADK}}(t)$, which is obtained using instantaneous ADK rates. As discussed in [71], we find that for a given peak intensity the ionization probability $P_{\mathrm{ADK}}(t)$ calculated from ADK rates differs from $P_{\mathrm{vol}}(t)$ by only a constant factor β, as long as the intensity is below the ADK saturation intensity. We determine β as the ratio between $P_{\mathrm{vol}}(t)$ and $P_{\mathrm{ADK}}(t)$ at the

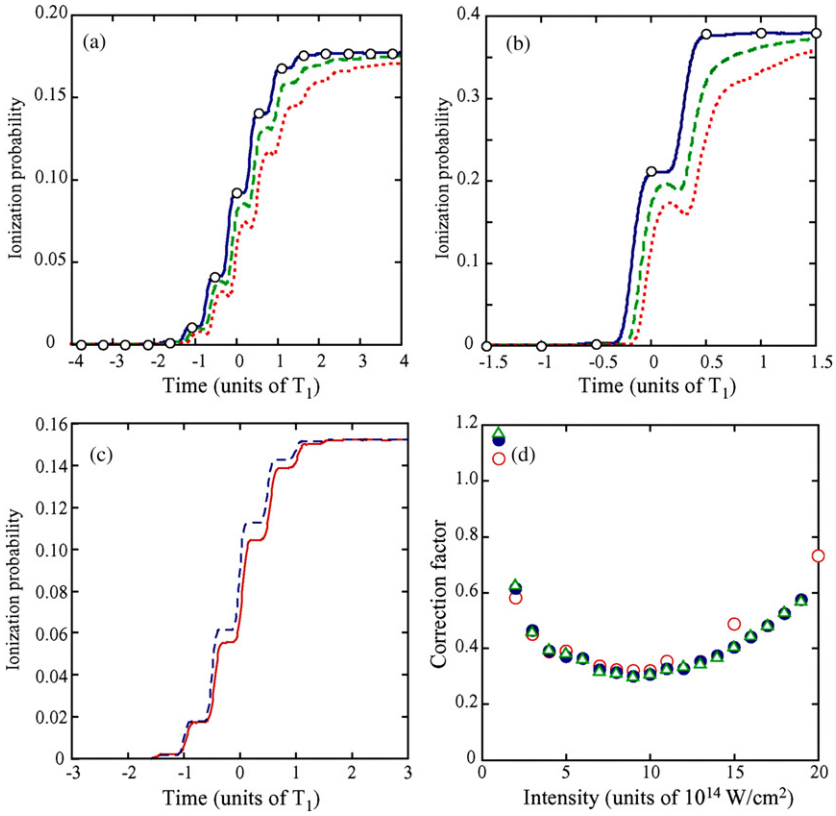

Figure 5. Time-dependent ionization probabilities for a neon atom exposed to a 750 nm laser pulse with a peak intensity of 10^{15} W cm^{-2}. In (a) and (b) we have used pulse durations of 7.5 fs and 2.5 fs, respectively, and show the result of using spheres with radius 10 au (solid line), 30 au (dashed line) and 50 au (dotted line) to define $P_{\rm vol}(t)$ in the numerical solution of the TDSE. We also show the ionization probability calculated from the population left in the ground state, which can be evaluated only when electric field is zero (open circles). (c) Time-dependent ionization probability of a neon atom exposed to a 750 nm, 7 fs laser pulse with a peak intensity of 10^{15} W cm^{-2}. $P_{\rm vol}(t)$ is shown with solid line, $\beta P_{\rm ADK}(t)$ is shown with dashed line. $T_1 = 2.5$ fs is the optical period of the driving field. (d) Intensity-dependent correction factor β for three different pulses: 7 fs duration, cosine carrier (open circles); 5 fs duration, cosine carrier (open triangles); 5 fs duration, sine carrier (filled circles).

end of the laser pulse. Figure 5(c) shows a typical example of the excellent agreement between $P_{\rm vol}(t)$ and $\beta P_{\rm ADK}(t)$, for a 750 nm, 7 fs driving pulse with a peak intensity of 10^{15} W cm^{-2}. The ionization probability at the end of the pulse is only about 15%. In figure 5(d) we show the intensity dependence of the correction factor, $\beta(I_0)$. The insensitivity of $\beta(I_0)$ to the duration and phase of the driving pulse ensures that this correction is justified even as the pulse changes shape and phase during propagation. Finally, we use $\beta(I_0)P_{\rm ADK}(t)$ to calculate the source terms $N_e(t)$ and $\gamma(t)$ for each point in the nonlinear medium, where I_0 is the peak intensity of the driving pulse at that point.

This latter correction method was used in the calculation shown in figure 4, and in the results on ionization driven spatio-temporal reshaping in neon shown in section 4.5.

In the long-pulse (adiabatic) regime, several groups have successfully implemented Coulomb corrections to rates calculated within strong-field-type approximations [82–86].

3.2.2. Dipole source term for the generated fields. The source term for the generated XUV radiation is calculated from the time-dependent nonlinear polarization field, which is taken to be proportional to the microscopic single-atom dipole moment $x_{nl}(t)$ and the density of neutral atoms,

$$\tilde{P}_{\rm dip}(\omega) = \widetilde{FT}[N_{\rm atom}(t)x_{nl}(t)], \tag{17}$$

where $\widetilde{FT}$ denotes a Fourier transform. Both the atomic density and the dipole moment also depend on r and z. We calculate the time-dependent dipole moment by solving the TDSE, using a non-adiabatic form of the strong field approximation (SFA) [21] which takes into account the full time dependence of the driving field $E_1(t)$ [75] (in atomic units),

$$x_{nl}(t) = 2\,{\rm Re}\left\{{\rm i}\int_{-\infty}^{t} {\rm d}t'\left(\frac{\pi}{\epsilon + {\rm i}(t-t')/2}\right)^{3/2} d^*[p_{\rm st}(t',t) + A(t)]d[p_{\rm st}(t',t) + A(t')]\exp[-{\rm i}S_{\rm st}(t',t)]E_1(t')\right\}, \tag{18}$$

where ϵ is a small positive regularization constant, $A(t)$ is the vector potential associated with the electric field $E_1(t)$, and $d(p)$ is the dipole matrix element for transition between the ground state and a continuum state with momentum p, and is given by (for hydrogen-like atoms) [21]

$$d(p) = {\rm i}\frac{2^{7/2}(2I_{\rm p})^{5/4}}{\pi}\frac{p}{(p^2+2I_{\rm p})^3}. \tag{19}$$

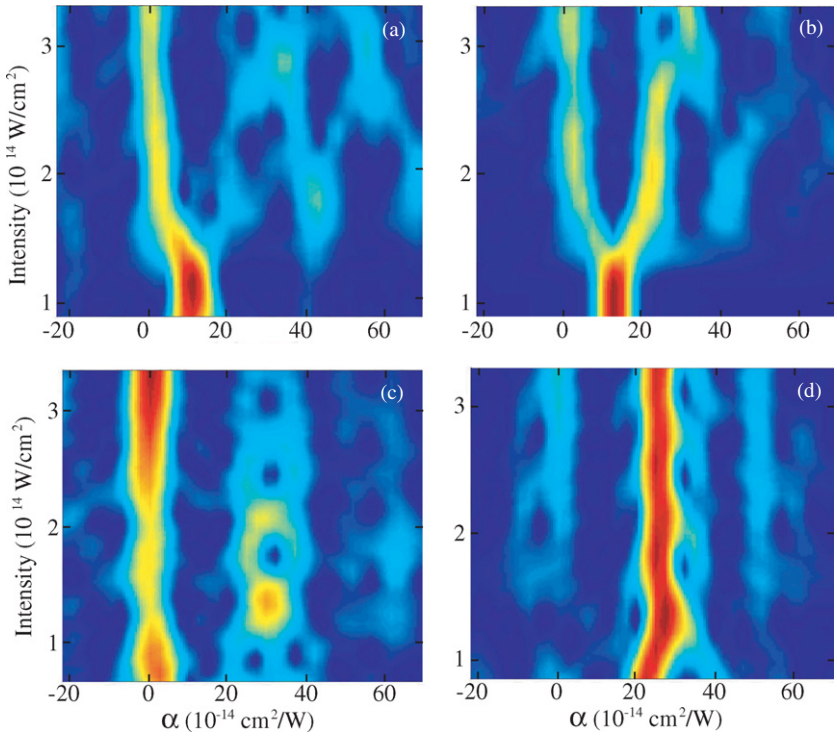

Figure 6. Quantum path contributions as functions of intensity for the 27th and 15th harmonics in argon (top and bottom row, respectively). (a) and (c) were calculated by numerical integration of the TDSE, (b) and (d) were calculated with the SFA. Note that what is labelled α on the x-axis in the figure is termed γ in the text for consistency with our definition of the phase coefficient in section 2. Reprinted with permission from [88]. Copyright (2002) by the American Physical Society.

As first proposed by Lewenstein *et al* [21], one can interpret the dipole radiation at time t as being a sum over all possible quantum paths characterized by an electron being released via tunnel ionization at the core at time t', and returning to the core at time t with kinetic energy $(p_{\rm st}(t', t) + A(t))^2/2$. The stationary values of the momentum $p_{\rm st}(t', t)$ and action integral along the trajectory $S_{\rm st}(t', t)$ are given by

$$p_{\rm st}(t', t) = \frac{1}{t' - t} \int_{t'}^{t} A(t'')\, {\rm d}t'' \tag{20}$$

$$S_{\rm st}(t', t) = (t - t')\big(I_{\rm p} - p_{\rm st}^2/2\big) + \frac{1}{2} \int_{t'}^{t} A^2(t'')\, {\rm d}t'', \tag{21}$$

where $I_{\rm p}$ is the atomic ionization potential. For a monochromatic field with a constant intensity, the stationary action is given by $I_{\rm p}(t - t') + U_{\rm p} f(t - t')$ where $f(t - t')$ is a function that depends only on the electron travel time $\tau = t - t'$. For return energies below the classical maximum of $3.17U_{\rm p}$, the stationary action quantum paths in the SFA are similar to the returning electron trajectories in the classical model discussed in the introduction, in terms of their release and return times and their phase coefficients α_j [24, 25, 61, 87]. The two quantum paths with travel time τ less than one cycle dominate the SFA dipole response at most intensities as discussed in more detail in connection with figure 6.

3.2.3. Validity of the strong-field approximation. At this point it is interesting to note that the dominant electron trajectories discussed in classical terms in the introduction, and as the stationary points of the SFA action integral, can also be recognized in more accurate (and more computationally intensive) numerical solutions of the 3D SAE-TDSE. In [88], Gaarde and Schafer calculated dipole radiation spectra for argon and neon via direct numerical integration of the SAE-TDSE, using realistic pseudopotentials for the interaction between the active electron and the ion core [89]. They calculated harmonic spectra for many quasi-constant peak intensities to obtain $d_q(I)$, the intensity-dependent strength of the dipole spectrum for each harmonic q. The intensity-dependent dipole moment was then analysed in terms of its conjugate variable, the phase coefficient γ, in the following way [90]:

$$D_q(\gamma, I_0) = \int {\rm d}_q(I) W(I_0)\, {\rm e}^{{\rm i}\gamma I}\, {\rm d}I, \tag{22}$$

where $W(I_0)$ is a window function centred on intensity I_0. For each intensity I_0, the magnitude of $D_q(\gamma)$ represents the weight of the contribution with phase coefficient γ to the dipole moment of harmonic q. The resulting distribution of phase coefficients as a function of intensity I_0 for two harmonics in argon is shown in figure 6. We note that in this representation of the intensity-dependent phase, the phase coefficient γ is proportional to the laser wavelength to the third power, in contrast to the wavelength independent expression of the phase coefficient α discussed in section 2.

At the lowest intensities, the 27th harmonic is in the cutoff region and there is only one dominant phase contribution (corresponding to only one quantum path). At higher

intensities this path splits into two, with phase coefficients as predicted by the semi-classical model. At an intensity of about 1.5×10^{14} W cm^{-2} a second group of phase coefficients appear (corresponding to quantum paths with travel times longer than one optical cycle) which bifurcates into two paths above 2×10^{14} W cm^{-2}. It is clear that for both the 27th and the 15th harmonic in argon the shortest path (with the smallest γ) dominates the response.

Figure 6 also shows the SFA predictions for the phase coefficients in the 27th and 15th harmonics in argon. Comparison between the TDSE and the SFA results shows that although the SFA agrees well with the TDSE in terms of *which* quantum paths contribute to the dipole moment, the prediction for their relative *weight* is quite different. In particular, the SFA strongly favours the second-shortest quantum path (which in the literature is often referred to as the 'long' quantum path), whereas the more accurate calculation predicts that the shortest path is the more dominant, and that the short path of the second group of trajectories contributes as much as or more than the long path of the first group of trajectories. Gaarde and Schafer discussed in [88] that this result is quite general and true for many harmonics in both argon and neon. Recent work by Tate and collaborators has shown that for driving fields with wavelengths in the mid-infrared range, quantum paths longer than one optical cycle are even more important than at 800 nm [27]. Gaarde and Schafer have also found that the overall yields of the dipole moments calculated within the SFA (using 800 nm driving laser pulses) are somewhat lower than the SAE results. At low intensity, when a harmonic is in the cutoff region, the two calculations agree well. At higher intensity, when a harmonic is deep in the plateau region, the SFA can underestimate the harmonic strength by up to a factor of 10.

Propagation calculations based on using SAE-TDSE dipole moments have given results that are in very good qualitative and quantitative agreement with experimental results for harmonic generation driven by long pulses (these propagation calculations are based on the slowly varying envelope approximation), see for instance [57, 91]. We therefore believe that comparison with SAE-TDSE calculations can serve as a benchmark for more tractable but approximate calculations, such as the SFA, of the time-dependent dipole moments. For large-scale calculations incorporating accurate numerical solutions of the TDSE into non-adiabatic solutions of the MWE, see the work by Shon *et al* [76] and Lorin *et al* [74, 92].

The conclusion that one should draw from the comparison shown in figure 6 is that SFA-based predictions about the generation and properties of high harmonics and attosecond pulses should be made with caution. In many experimental scenarios, phase matching conditions are such that only one quantum path contribution really matters (usually the short one which leads to XUV light with better temporal and spatial coherence properties) in which case the SFA can serve adequately as the basis for predictions and interpretations [25, 87]. However, in cases where the phase matching restrictions are not severe enough to completely eliminate one or more trajectories, so that there are substantial contributions from longer trajectories, SFA predictions can be misleading,

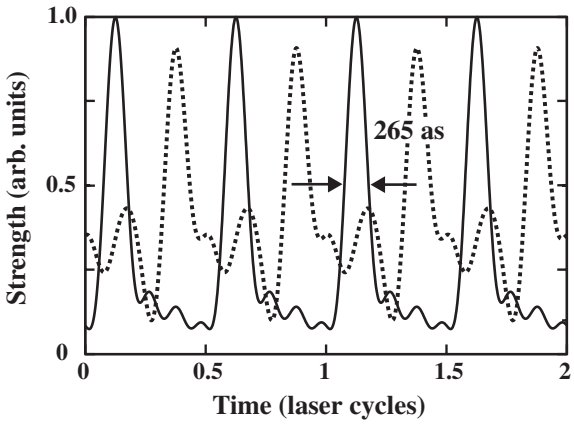

Figure 7. Time profile of harmonics 15–23 in argon after propagation through a 1 mm argon gas jet at low pressure, generated by a 810 nm, 100 fs driving pulse with a peak intensity of 2.5×10^{14} W cm^{-2}. The confocal parameter of the beam was 5 mm, and the gas jet was placed 2.5 mm beyond the laser focus. These parameters are similar to those used in the experiment by Paul and collaborators [2]. Results of using TDSE or SFA dipole data are shown with solid or dashed lines, respectively. Reprinted with permission from [88]. Copyright (2002) by the American Physical Society.

see for instance [57, 93, 59]. An example of this, for the generation of a train of attosecond pulses from low-order harmonics in argon, is shown in figure 7.

3.3. Implementation of propagation equations

So far we have described the calculation of atomic quantities from a one-electron atom. For argon, neon and helium, the two $m = 0$ electrons in the outermost shell contribute equally to the depletion of the ground state and the dipole radiation (and the $m = \pm 1$ electrons in argon and neon ionize and contribute at a much lower rate because their orbitals are not aligned with the laser field). The time-dependent macroscopic polarization field $P_{\text{dip}}(t)$ is thus given by

$$P_{\text{dip}}(t) = 2N_0(1 - P_{\text{ion}}(t))x_{nl}(t), \tag{23}$$

where N_0 is the initial atomic density and $p_{\text{ion}}(t)$ is the one-electron ionization probability, which is related to the probability for an atom to stay neutral, $P_{\text{neutral}}(t)$, by

$$p_{\text{neutral}}(t) = (1 - p_{\text{ion}}(t))^2. \tag{24}$$

The macroscopic density of free electrons is then given by $N_{\text{el}}(t) = N_0(1 - p_{\text{neutral}}(t))$.

The nonlinear medium is initially defined by its ionization potential and the initial atomic density. We usually assume that the density of the medium is constant in the radial direction (which is a very reasonable assumption since the laser waist is usually on the order of 100 μm or less), and also in the z-direction except for a linear increase and decrease at the edges. It would be straightforward to implement a different gas profile if so desired. The length of the medium in the z-direction is typically between 0.5 mm and 5 mm.

The driving field is specified both in terms of its temporal and spatial properties. We define an initial pulse by its

wavelength, its pulse duration τ at FWHM, and the peak intensity it would have in the focus if it were propagating in vacuum. The intensity envelope for the initial pulse is usually given by a $\cos^4(at/\tau)$ function where a is defined so that $\cos^4(a/2) = 0.5$. The time resolution is set by the highest frequency one wishes to resolve in the harmonic spectrum, typically a few hundred points per optical cycle of the driving field. To get sufficient frequency resolution for the propagation of both the laser and the harmonic fields we pad the time axis with zeros before and after the pulse. The time axis typically spans from -4τ to $+4\tau$, and the total number of points in the time and frequency domain is on the order of 10^4.

The initial spatial profile of the laser beam is a Gaussian and is specified in the frequency domain by its confocal parameter and the position of its focus relative to the centre of the nonlinear medium. We specify the confocal parameter of the central frequency of the pulse, and assume that all other frequencies in the spectrum are focused with the same lens (which means that the confocal parameter varies proportionately with the frequency). We typically use between 200 and 400 points in the radial direction, and between 100 and 400 points in the propagation direction, depending on the relative lengths of the medium and the confocal parameter, and the laser peak intensity.

The only computationally expensive quantity is the evaluation of the time-dependent dipole moment in equation (18), since for each time t it involves an integral over all previous times t' where electrons could have been released into the continuum. In principle, it even involves a double integral since the stationary momentum and action are defined from integrals of $A(t'')$ and $A^2(t'')$ between t' and t. We reduce the computation time in a number of ways.

- We pre-calculate the integrals $f_{A1}(t) = \int_{-\infty}^{t} A(t')\,\mathrm{d}t'$ and $f_{A2}(t) = \int_{-\infty}^{t} A^2(t')\,\mathrm{d}t'$. The stationary momentum $p_{\mathrm{st}}(t,'t)$, for instance, is then given by $(f_{A1}(t) - f_{A1}(t'))/(t' - t)$.
- For any given time t, we only start the t' integral at release times t' equal to one or two cycles before t. This means we are only including trajectories with return times that are shorter than one (or two) optical cycles. Since the SFA response is dominated by the trajectories that return within one cycle, this usually gives a very good agreement with longer integration times.
- We only evaluate the dipole moment over the part of the time axis where the electric field is nonzero. The electric field is only exactly zero on the zero-padded part of the time axis right at the beginning of the medium. As soon as it starts propagating, both physical and numerical effects cause it to 'spill' over onto the time axis where it was previously zero. However, since the contribution to the dipole moment is negligible at very low electric fields, this is not usually a problem.
- We only calculate the dipole moment over part of the radial profile where the peak intensity of the driving field is non-perturbative. Depending on the atomic species, we choose a minimum peak intensity typically around 10^{13} W cm^{-2}. For grid-points in the radial direction where the temporal peak intensity is less than this intensity, we do not calculate the time-dependent dipole moment with the SFA formalism. Instead we assume a perturbative decrease with intensity, which we evaluate in the frequency domain.
- As discussed in [75], we do not calculate the time-dependent dipole moment at each step in the propagation direction, as the driving field intensity is usually slowly varying. We typically evaluate it every five or ten steps, depending on how rapidly the driving and generated fields are evolving due to effects of ionization and phase matching. At the steps in between we scale the response to correct for any change in atomic density, and correct for the evolution of the driving field phase due to propagation. If the intensity is high it can be necessary to calculate the ionization source terms for the laser field at each step, but this is not nearly as time consuming as the calculation of the time-dependent dipole moment.

4. Results

In the following we will review a range of different schemes for attosecond pulse production, in each case focusing on the interplay between the microscopic and macroscopic aspects of the generation process. For each scheme we will highlight the temporal, spectral and spatial gates that enables the temporal and spatial isolation of attosecond XUV pulses at the detector or target. In some (most) schemes, macroscopic effects are crucial in the time gating process, whereas in a few schemes that rely on a single-atom time gating mechanism, macroscopic effects must be kept to a minimum to preserve the single-atom nature of the interaction over the entire interaction volume.

We will start by discussing the first and best known example of macroscopic time gating in attosecond pulse generation: the macroscopic separation of the two quantum path contributions to the single-atom dipole moment as first discussed by Antoine and collaborators [26] in the context of generating trains of attosecond pulses (section 4.1). We will then discuss the generation of isolated attosecond pulses using few-cycle driving pulses (section 4.2), and using few-cycle pulses in combination with polarization gating (section 4.3). In sections 4.5 and 4.6, we show two examples of how macroscopic effects can isolate a single attosecond pulse in space and time from a longer XUV pulse generated by a multi-cycle driving pulse. In section 4.7, we discuss how the generation of harmonics and attosecond pulses by driving lasers with wavelengths in the mid-IR regime (1.5–3 μm) is extremely sensitive to phase matching conditions because of the increase in the intensity-dependent phase variation with laser wavelength. Finally, in section 4.8 we discuss how a two-colour driving field provides an additional single-atom temporal gate in attosecond pulse production, and how to extend this single-atom control to the macroscopic domain.

4.1. Phase matching driven selection of microscopic quantum path contributions

The best known example of the influence of macroscopic effects on the generation of harmonics and attosecond pulses is the phase-matching controlled separation of the different

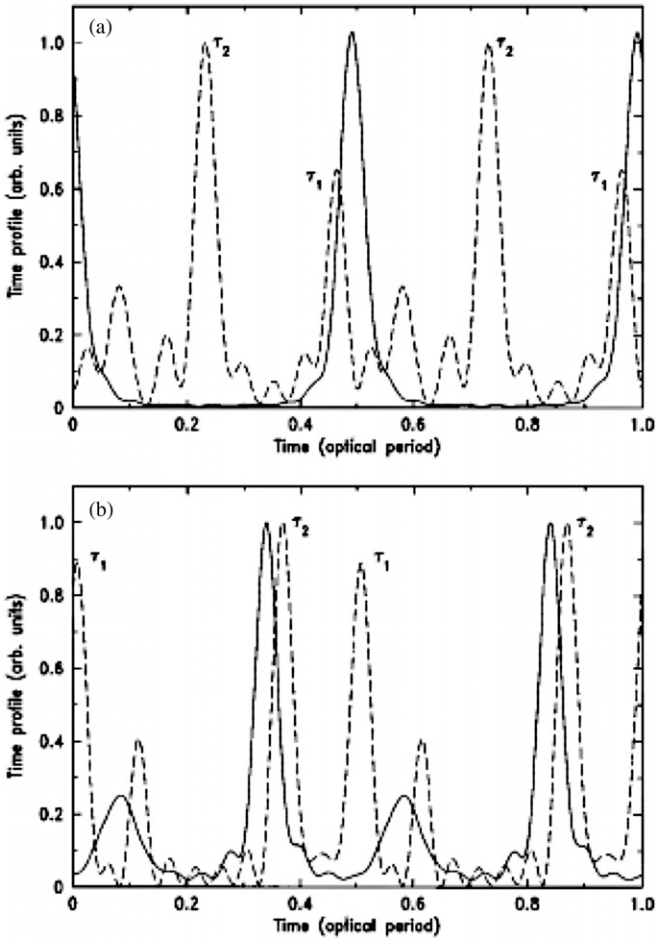

Figure 8. Macroscopic time profiles of harmonics 41–61 in neon for two different focusing conditions, favouring either short or long trajectory (solid lines). Shown with dashed lines are the single-atom time profiles (shifted in time to account for different Guoy phases due to different focusing conditions). The intensity of the 825 nm laser field was 6.6×10^{14} W cm^{-2} and the confocal parameter was 5 mm. In (a) the nonlinear medium was placed a few millimetres after the laser focus, to optimize the contribution of the short quantum path, labelled τ_1 in the figure, in (b) the medium was placed very close to the laser focus to optimize the long-path contribution, labelled τ_2. The calculations were performed in the long-pulse (adiabatic) limit. Reprinted with permission from [26]. Copyright (1996) by the American Physical Society.

quantum path contributions to the single-atom dipole moment. This was first demonstrated in calculations by Antoine and coworkers [26] in the context of generating trains of attosecond pulses by a long IR pulse in neon. In the single-atom response, even after spectrally selecting a range of harmonics in the plateau region, the resulting train of attosecond pulses always exhibits at least two attosecond bursts per half-cycle, corresponding to the emission times for the two shortest electron trajectories discussed above (see figure 1). Antoine *et al* showed, as in figure 8, that in the macroscopic response it is possible to synthesize trains with just one attosecond pulse per half-cycle. By changing the focusing conditions of the driving laser beam (specifically, by moving the laser focus relative to the centre of the gas jet) they were able to phase match the contribution from either the short or the long electron trajectory [26]. In this scheme for attosecond pulse generation, a *temporal gate* is formed in each half cycle of the field by *phase matching*, leaving a train of attosecond pulses with only one burst per half-cycle.

This selection of a microscopic quantum path contribution via the macroscopic effect of phase matching can be understood using phase matching maps such as those shown in figure 3. The harmonics that were used to make the attosecond pulse trains in figure 8 were all from the mid-plateau range, corresponding to the harmonics in figure 3(a)–(d). For these harmonics, the short-path contribution is well phase matched when the nonlinear medium is placed a few millimetre after the laser focus. The long-path contribution to a smaller range of plateau harmonics is well phase matched on or off axis when a short medium is placed close to the laser focus. Both of these observations are in agreement with the results of figure 8: the isolation of the short trajectory contribution in figure 8(a) was very efficiently achieved by placing the neon gas a few millimetre after the laser focus, and the less effective isolation of the long trajectory contribution in figure 8(b) was achieved by placing the neon gas very close to the laser focus.

There is another and conceptually simpler way to macroscopically select one or the other quantum path contribution. As was first experimentally demonstrated by Bellini and collaborators, a *spatial filter* placed in the far field may act as a *temporal gate* and separate the two quantum path contributions [57]. The origin of the spatial separation is once again the different intensity-dependent phase variations of the two contributions, which means that the electric field generated by each contribution will have phase fronts with very different curvatures and therefore different divergences. The arrows in figure 3 indicate the direction of the wave vector $\vec{k}_{\text{source}}$ which is imposed on the harmonic field by the laser field at each point. Clearly, the contributions from the long trajectory are much more divergent than those of the short trajectory. This means that in the far field, one can separate the short and long trajectory contribution with a small aperture. An example from Bellini *et al* is shown in figure 9 for the 15th harmonic in argon. By measuring the coherence time of the harmonic pulses, Bellini and coworkers demonstrated that the bright, narrow spot in the centre is due to the short trajectory and the weaker, more divergent, radiation off axis is due to longer trajectories [57]. The macroscopically driven far-field separation of microscopic quantum path contributions has since then been explored in great detail and is standardly employed in a range of experiments [2, 25, 59, 87, 93, 94].

We note that in the first experimental demonstration of an attosecond pulse train from harmonics 11 through 19 in argon, Paul and collaborators employed both phase matching and spatial gating, by placing the argon medium a few millimetre after the laser focus and having a small aperture in the far field to select only the collimated part of the XUV radiation [2].

4.1.1. Macroscopic control of individual pulse durations in attosecond pulse trains. The duration of individual bursts in an attosecond pulse train (APT), even after macroscopic selection of only one quantum path contribution, is limited both by the spectral range of harmonics used to synthesize the

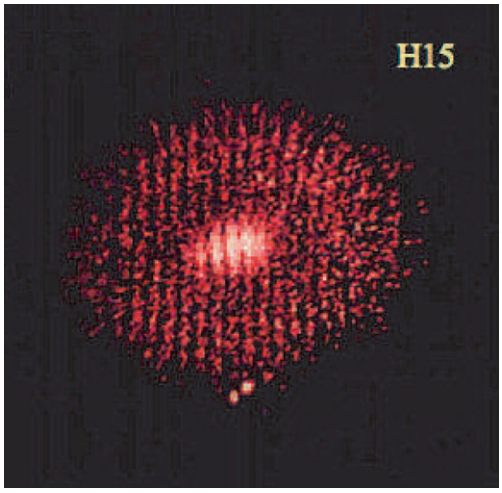

Figure 9. Spatial profile of the 15th harmonic in argon in the far field, showing different quantum path contributions spatially separated via phase matching. The interference pattern visible in both the inner and outer part of the beam is due to an identical, time-delayed harmonic pulse which was used to measure the coherence times of the inner and outer parts of the beam.

train and by the variation of the single-atom dynamics over this photon energy range, see for instance [11, 27, 61, 62, 94]. This is because the different XUV energies constituting the bandwidth of the train are made by electron trajectories with slightly different times of return. For the short quantum path, the highest energies are made by trajectories that spend longer time in the continuum and return later to the core, giving rise to the so-called atto-chirp of the individual attosecond pulses in the train [61, 62]. López-Martens and collaborators showed that the atto-chirp can be macroscopically compensated by sending the APT through a medium with a negative dispersion which induces a delay of the lowest energies in the train with respect to the highest energies in the train [94]. In this way, APT pulses synthesized from harmonics 13–35 in argon were compressed from an initial duration of 480 as to 170 as, very close to the Fourier transform limit.

More recently, Ruchon and collaborators have shown that it is possible to macroscopically minimize the atto-chirp directly during the harmonic generation process [67]. They show that in very loose focusing conditions, where the effects of focusing and the intensity-dependent dipole phase are minimal, the dispersion induced by the presence of free electrons ionized during the harmonic generation and the dispersion induced by the neutral atoms in the gas can compensate each other over a range of harmonic energies, since one increases and the other decreases with increasing photon energy. Their measurements of the atto-chirp support the conclusion from calculations that there is an optimum pressure and ionization fraction for the production of transform limited bursts in the APT [67].

4.2. *Few-cycle driving pulses*

Conceptually, spectral filtering of the high harmonic spectrum generated by a few-cycle driving pulse is the simplest scheme for producing isolated attosecond pulses [4, 5, 28–32]. In general, the highest harmonic energies are only generated at the peak of the pulse and if the driving pulse is short enough (approximately two optical cycles or less) and has the appropriate carrier envelope phase (CEP), the XUV radiation in the cutoff region can be emitted during one half-cycle only, producing a continuous spectrum. This method has been demonstrated experimentally by the group of Krausz and collaborators [4, 5], yielding isolated attosecond pulses with durations of a few hundred attoseconds. Technically, this approach to single attosecond pulse generation is very demanding as it requires access to intense, phase stabilized, sub-6 fs laser pulses [95].

The XUV time gate is formed in this case by the combination of a short pulse (intensity gate) and a spectral filter (spectral gate) and is single atom in nature—each atom is emitting the highest frequencies during an intensity gate that only lasts a short time. Macroscopic effects are important mainly in terms of the yield and coherence properties of the attosecond pulses—it is important that the macroscopic effects work to enhance and not destroy the single-atom gating mechanism. In addition, as we discussed earlier, it is only for a few cycle driving pulse that one can achieve non-adiabatic self-phase matching for very high XUV energies, for which phase matching would otherwise be strongly limited by the presence of free electrons [19, 72].

4.2.1. Isolated attosecond pulses from molecules driven by few-cycle laser pulses. Very recently, Lorin and collaborators have reported interesting propagation effects in calculations of isolated attosecond pulse production by a macroscopic number of aligned H_2^+ ions driven by an intense, few-cycle 800 nm laser pulse [92]. They see that for high molecular densities, the harmonic plateau extends to substantially higher energies than at lower densities, indicating the potential for synthesizing shorter attosecond pulses. They attribute the extension of the plateau to a spectral broadening of the laser pulse towards lower frequencies during propagation through the gas, due to self-phase modulation (the Kerr effect) [92].

4.2.2. Few-cycle pulses produced via filamentation. Several groups have taken an interest in using few-cycle pulses produced via self-compression during laser-driven filamentation for driving strong field processes [96, 97], as an alternative to the more standard few-cycle pulses produced in hollow-core fibres [95]. Chakraborty *et al* have recently shown in calculations that isolated attosecond pulses can be produced from cutoff harmonics generated by these self-compressed filaments, and that the sub-femtosecond XUV time gate for these pulses is formed by the (standard) steep intensity gate at the rising edge of the pulse, and by a steep frequency gate at the peak and trailing edge of the driving pulse. This frequency gate arises because of a large blue shift imposed on the laser pulse during the filamentation process, which rapidly lowers the instantaneous cutoff energy [98].

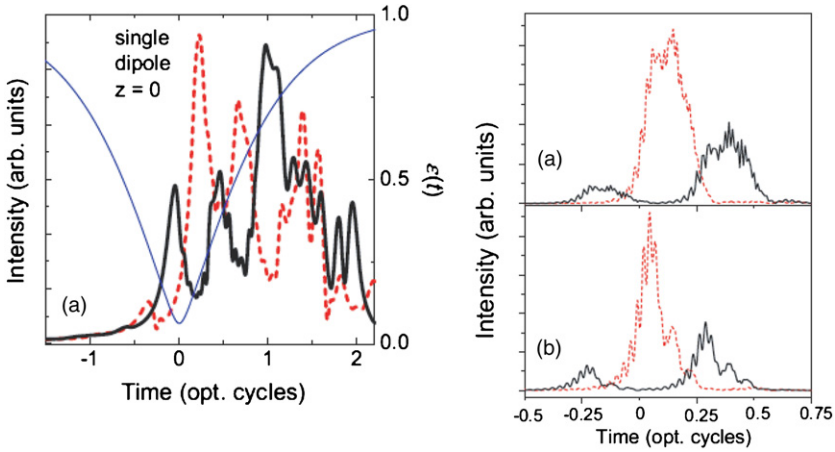

Figure 10. Left panel: single-atom time profile of harmonics in argon between 25–45 eV generated by a 750 nm, 5 fs driving pulse with a rapidly varying ellipticity (shown in the figure with thin solid line). Results of using two different values of the CEP are shown with thick solid or dashed lines. The XUV emission is clearly not of sub-femtosecond duration. The peak intensity of the driving pulse during the linearly polarized gate is approximately 5×10^{14} W cm^{-2}. Right panels: (a) and (b) on axis and radially integrated time profiles of harmonics in the same range after propagation through a 1 mm long argon gas jet at a pressure of 30 mbar. Reprinted with permission from [41]. Copyright (2007) by the American Physical Society.

4.3. Polarization gating

Recently, the production of an isolated attosecond pulse via polarization gating of high-order harmonics generated by a short driving pulse has been experimentally demonstrated [33, 34]. The time-gating mechanism of this approach is based on the strong sensitivity of the harmonic generation process to the polarization (ellipticity) of the driving laser pulse [35–40, 99]. Harmonic generation is very inefficient even for small ellipticities of the laser field, and by constructing a laser pulse in which the light is linearly polarized only during a single half-cycle one forms a polarization gate for the generation of an isolated attosecond pulse. The advantage of the polarization gate as compared to the intensity/time gate discussed above is that in principle a much larger range of frequencies in the harmonic spectrum will be emitted during a short time (not only the frequencies in the cutoff region), allowing for potentially much shorter attosecond pulses with higher yields. In the experiment by Sansone and collaborators, the sub-cycle polarization gate was produced by the combination of two CEP stabilized few-cycle (≈5 fs) pulses with orthogonal polarizations which were delayed with respect to each other [33, 34].

Very interestingly, it has recently been proposed by Altucci and collaborators [41] that the production of single attosecond pulses via polarization gating is actually a *macroscopic* effect of phase matching in the nonlinear medium and not a single-atom ellipticity gating effect. Their calculations show that the electron trajectories that are initiated, accelerated and returned to the core by an electric field with a rapidly varying ellipticity are actually much longer than the trajectories in the linear polarization case, especially for lower harmonics far from the cutoff energy. The authors refer to these as 'super-long' trajectories. The single-atom emission time for a range of plateau harmonics in argon can therefore be substantially longer than the ellipticity gate itself, as shown in the left panel in figure 10, from [41].

The calculations of Altucci *et al* also show that it is the effects of phase matching and radial averaging during propagation through a macroscopic nonlinear medium that allows the generation of an isolated attosecond pulse, as shown in the bottom right panel of figure 10. The 'super-long' trajectories are suppressed due to a lack of phase matching, and the off-axis contributions to the range of harmonics considered are emitted during a shorter time than the on-axis contributions. Altucci and collaborators point out that their calculations are in good agreement with the experimental measurements of isolated attosecond pulses produced in polarization gates, in terms of the parameters used in the experiments and the durations measured [33, 34, 41].

4.4. Production of isolated attosecond bursts by driving pulses longer than two optical cycles

There is currently great interest in experimental schemes that would produce isolated attosecond pulses without starting from intense, CEP stabilized, two-cycle (5 fs) driving pulses which are notoriously hard to produce and control. To produce an isolated attosecond burst with pulses that are longer than two optical cycles, the generation scheme must give rise to additional time gating mechanisms beyond the intensity gate provided by the peak of the pulse. The following four sections discuss different such generation schemes, many of them relying on macroscopic effects such as ionization and phase matching to provide the extra XUV time gating mechanism.

4.5. Spatio-temporal gating of isolated attosecond pulses based on ionization-driven reshaping

Gaarde and Schafer recently demonstrated that macroscopic effects can play a crucial role in the production of isolated attosecond pulses by a pulse substantially longer than two optical cycles [42]. They performed detailed

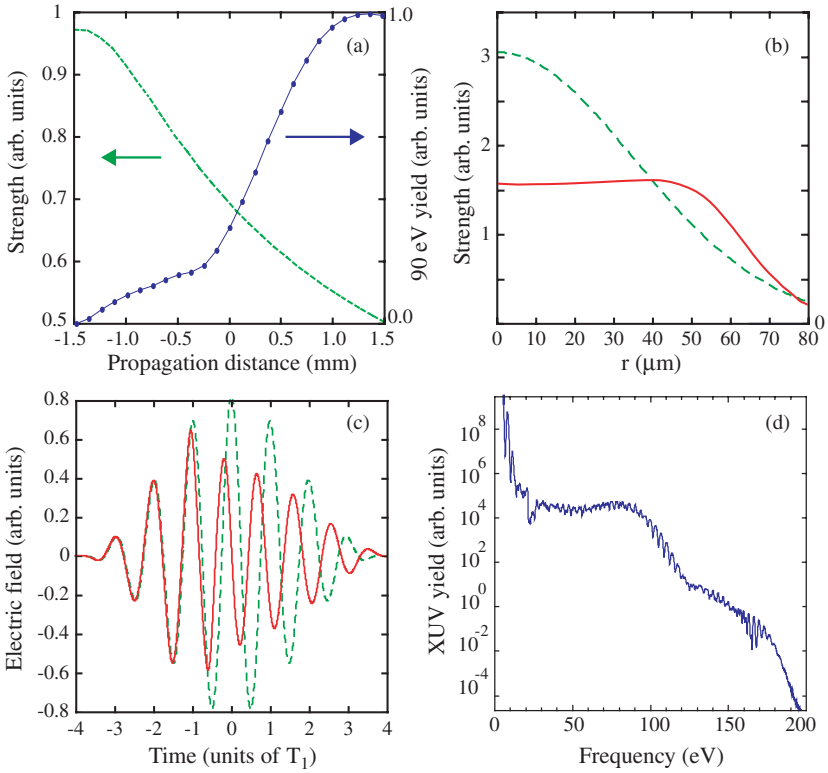

Figure 11. Spatio-temporal dynamics of the propagation of a 750 nm, 7 fs pulse, with an initial peak intensity of 9×10^{14} W cm^{-2} propagating through 3 mm of neon gas at a pressure of 150 Torr. (a) shows the on-axis energy density of the driving field (dashed line, left axis), and the radially integrated yield of the generated radiation around 90 eV (symbols, right axis) as a function of propagation distance. In (b) we compare the radial intensity distribution, and in (c) the on-axis time-dependent electric field, at the beginning and at the end of the medium (dashed and solid lines, respectively). In (d) we show the radially integrated harmonic spectrum at the end of the neon gas. The high-energy cutoff which can be seen around 175 eV is from radiation which is generated only at the beginning of the neon gas where the intensity is still high [71].

numerical simulations of the 2001 experiment in which isolated attosecond pulses were first detected [1]—somewhat surprisingly generated by an almost three cycle long pulse which was not CEP stabilized. Gaarde and Schafer found that ionization driven spatio-temporal reshaping of an intense driving pulse as it propagates through a long, relatively dense medium leads to XUV radiation which, after spatial and spectral filtering in the far field, yields an isolated attosecond pulse. The XUV time gating mechanism in this case is provided by a spectral and spatial filter, the effectiveness of which is enabled by the ionization driven reshaping of the laser pulse that happens during its propagation through the medium.

The focusing conditions of the driving laser beam employed in the experiment in [1] and the calculations in [42] were very loose (confocal parameter ten times longer than the nonlinear medium) which means that it is ionization effects that dominate the propagation dynamics, and the effects of phase matching as discussed in the context of figure 3 are minimized. Figure 11 illustrates some of the spatio-temporal dynamics that can be caused by rapid ionization in a relatively dense medium. We show the evolution of a 750 nm, 7 fs laser pulse as it propagates through a 3 mm long neon gas medium with an atomic density of 5×10^{18} cm^{-3}. The focusing conditions are very loose, with an initial confocal parameter of more than 4 cm. The peak intensity in the centre of the focus (in the absence of ionization-induced defocusing) would be 9×10^{14} W cm^{-2}. Although ionization is far from saturated at the end of this pulse (the one-electron ionization probability is 15% at the end of the pulse), it plays a profound role in the propagation dynamics. The ionization probability is highest on axis because of the radial intensity variation of the focused beam, and the resulting radial variation of the electron density acts like a negative lens which rapidly defocuses the laser beam. The resulting lower intensity in turn slows down the defocusing process. Figure 11(a) shows the evolution of the on-axis energy density of the field as a function of propagation distance. The intensity on axis is reduced by about a factor of 2 by the end of the medium, and the radial profile is much wider and almost flat over a diameter of about 100 μm (shown in figure 11(b)). The largest changes to the spatial profile happen in the first half of the medium where the intensity is highest (since the ionization is highly nonlinear). Once the ionization probability is lowered to just a few per cent (which happens about half-way through the medium in these conditions), the spatial profile does not significantly change its shape but merely diverges slowly because it has acquired a diverging phase front.

The time dependence of the refractive index, through the variation of the electron density, leads to a time-dependent phase of the electric field and therefore a frequency chirp.

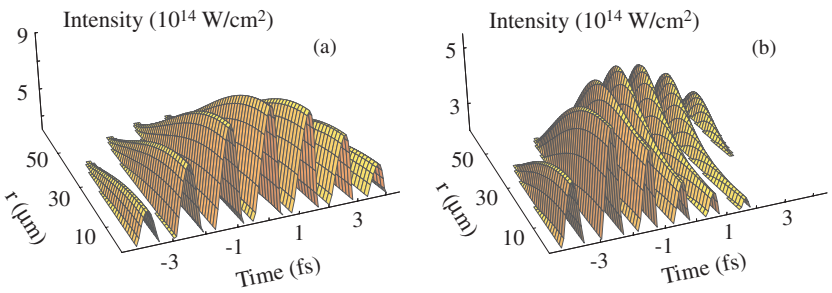

Figure 12. Spatio-temporal intensity profile of the laser pulse at the beginning (a) and at the end (b) of the neon gas in which XUV harmonics are generated. The initial peak intensity of the 750 nm, 7 fs laser pulse in (a) is 9×10^{14} W cm^{-2}. The CEP is zero. Note that the intensity scale is different in (a) and (b), and that it does not start at zero. Reprinted with permission from [42]. Copyright (2006) by the Optical Society of America.

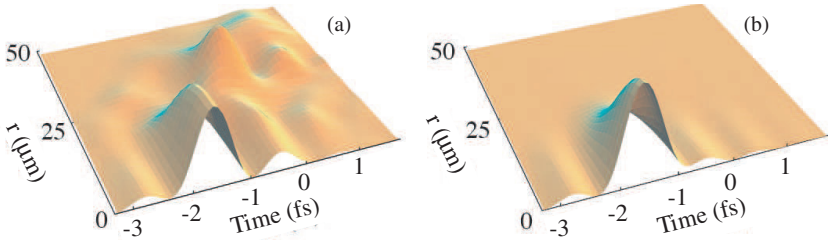

Figure 13. XUV generation resulting from the laser pulse shown in figure 12. We show the spatio-temporal profile of 90 eV radiation at the end of the neon gas (a) and in the focus generated after spatial filtering and reflection by a 2 mm diameter mirror placed 3.0 m from the neon source (b).

During the pulse the electron density either increases (when the intensity is high), or stays constant (when the intensity is low). Even if the intensity were sufficiently high to saturate the ionization probability, the electron density would initially increase and then saturate and stay constant. This means that the central frequency will always be blue shifted during propagation through an ionizing medium, and that the blue shift is in most cases time-dependent. Such a blue shift is evident in the comparison between the on-axis laser electric field at the beginning and at the end of the medium, shown in figure 11(c).

Figure 11(c) also shows that the electric field at the end of the medium has been reshaped temporally. The peak of the pulse occurs earlier and the effective duration of the on-axis pulse is shorter than the incoming pulse. This is an effect of the overall spatio-temporal reshaping that the laser pulse has undergone as demonstrated in figure 12, which shows its intensity profile at the beginning and at the end of the gas cell. The outgoing beam is much broader and more divergent than the incoming beam, and has a lower peak intensity. It also has a large radial phase variation which means that the peak intensity occurs at different times for different radial positions, and that the duration of the pulse varies with r.

The high-energy XUV radiation that emerges from the nonlinear medium in these conditions has been predominantly generated by the strongly reshaped laser pulse shown in figure 12(b) (see figure 11(a)), and individual XUV attosecond bursts are in general produced with different divergences. This is illustrated in figure 13, which shows the spatio-temporal intensity profile of the XUV radiation in a 5 eV window around 90 eV. Figure 13(a) shows the near-field XUV time profile at the end of the neon gas, whereas in figure 13(b) we have spatially filtered the XUV radiation by reflecting it on a small mirror placed on axis several metres from the gas, see [42] for details. Only the radiation with the smallest divergence is reflected by the mirror, resulting in a single attosecond burst in the focus (figure 13(b)). The duration of this pulse is 650 as and it contains an energy of approximately 3 pJ. This figure presents a very plausible explanation for why an isolated attosecond pulse could be produced by a 7.5 fs pulse by Krausz and collaborators [1].

The carrier envelope phase of the driving laser pulse in these calculations is zero with respect to a cosine oscillation. In [42] we explored the CEP dependence of the far-field selection of single attosecond pulses generated by a laser pulse with parameters as in figure 12, and showed that for most values of the CEP it is possible to isolate a single XUV burst. We also predicted that single attosecond pulses can be produced via spatial filtering by laser pulses as long as four optical cycles, if combined with CEP stabilization.

It is worth noting at this point that the ability of the far-field spatial filter to act as a temporal filter is a consequence of the ionization-driven reshaping of the laser pulse, and not a generic feature of far-field spatial filtering. In figure 14, we compare the radially integrated time profile of 90 eV radiation before and after far-field spatial filtering, generated by two different driving fields. In (a) we have used the same driving field as in figure 12, and in (b) the laser intensity is lower (5×10^{14} W cm^{-2}) and the confocal parameter is longer (6 cm). The duration for both laser pulses is 7 fs but their propagation dynamics are very different. The lower peak intensity pulse (b) propagates through the medium

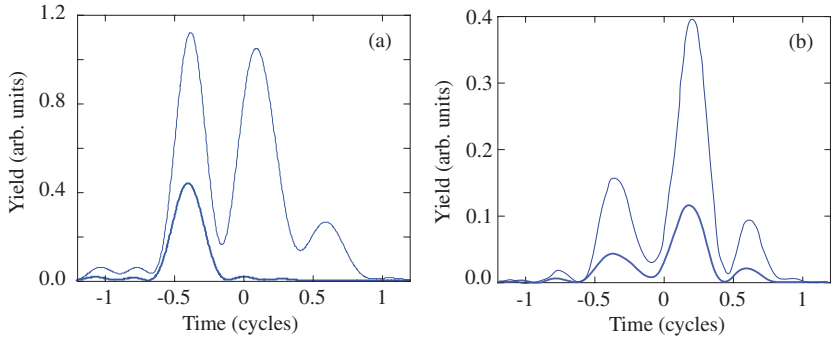

Figure 14. We compare radially integrated time profiles of 90 eV radiation at the end of the medium (thin lines) and after spatial filtering in the far field and refocusing to the near field (thick lines). In (a) we have used parameters as in figure 13, in (b) we have used a laser pulse with the same parameters except a lower initial peak intensity (5×10^{14} W cm^{-2}). The laser pulse in (b) gives rise to the same 90 eV cutoff energy as the one in (a), and the harmonic spectra from the two pulses are very similar. The pulse in (b), however, gives rise to very little ionization and does not undergo spatio-temporal reshaping.

essentially unaltered and the driving field intensity at the end of the medium is therefore similar for the two pulses. They both give rise to a harmonic cutoff energy around 90 eV and similar-looking harmonic spectra. The time profiles of the 90 eV radiation before far-field filtering both contain multiple attosecond bursts. However, spatial filtering does not alter the time structure of the XUV radiation generated by the laser pulse which has not undergone reshaping (b), it merely reduces it by an overall factor. This is because XUV bursts generated in consecutive half-cycles of the field in (b) will have similar divergence properties due to the smooth radial structure of the beam, and because the phase matching conditions do not change from one half-cycle to the next.

4.6. Spatio-temporal gating of isolated attosecond pulses based on phase matching

A different approach to spatial selection of an isolated attosecond XUV pulse was recently proposed by Haworth and collaborators in [43]. Their approach is based on the different phase matching that can be achieved for different energy regions of the harmonic spectrum in a tight focusing geometry. The authors calculate that in these conditions good phase matching on axis is only achieved for XUV radiation generated during one half-cycle of the driving field, and by applying a spatial and spectral filter in the far field they can temporally select a single attosecond pulse from a 3–4 cycle driving pulse. The extra XUV time gating mechanism in this case takes the form of a spatial and spectral filter, which is effective because of the large variation of the XUV phase matching conditions from one half-cycle to the next.

To understand how phase matching can provide a sub-femtosecond time gate, it is useful to start with a discussion of the concept of half-cycle cutoffs as introduced by Haworth and collaborators [43]. In a few-cycle pulse, which by its nature has a steep intensity gradient in each optical cycle, the peak electric field changes substantially from one half optical cycle to the next. This means that the maximum energy of the harmonic radiation also changes significantly from one half cycle to the next. These individual half-cycle cutoffs have been documented experimentally and were used by Haworth

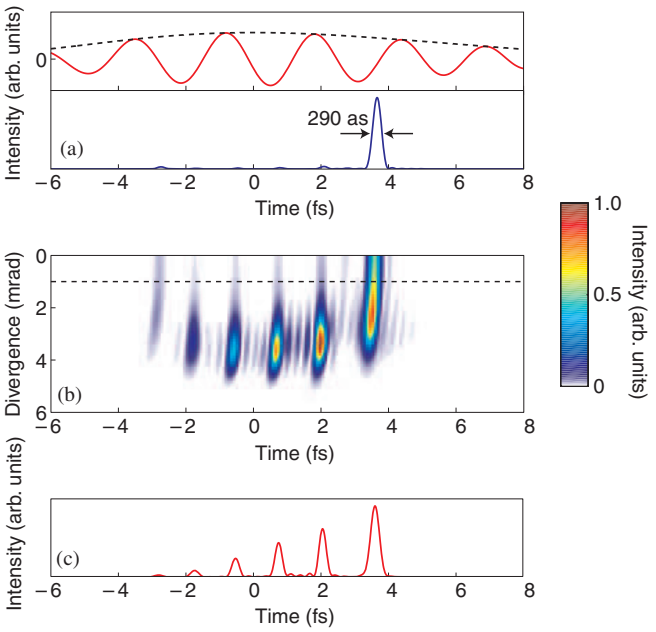

Figure 15. (b) Spatio-temporal behaviour of harmonic radiation around 90 eV, (c) before and (a) after spatial filtering with a narrow 2 mrad full-angle aperture. The time dependence of the driving electric field is shown in the top part of (a). See the text for the parameters of the calculation. Reprinted by permission from Macmillan Publishers Ltd: Nature Physics **3**, 52 (2007), copyright (2007) [43].

et al to measure the absolute phase of the driving laser field [43]. A given range of harmonics can thus belong to the plateau region during a half-cycle close to the peak of the pulse, and to the cutoff region during the next half-cycle with a lower peak intensity.

The phase-matching based spatio-spectral gating mechanism for producing isolated attosecond pulses proposed by Haworth *et al* is shown in figure 15. The figure shows the calculated macroscopic response of a 4 mm long gas of neon atoms at an atomic density of 3×10^{17} cm^{-3} (pressure of approx. 9 Torr) to an 8.5 fs, 800 nm laser pulse with a peak intensity of 6×10^{14} W cm^{-2}. The laser beam is focused relatively tightly compared to the length of the medium, with

a confocal parameter of 6 mm. Figure 15(b) shows the spatio-temporal intensity profile of the XUV radiation with photon energies close to 90 eV (13.5 nm) at the end of the neon gas. There are approximately four significant attosecond XUV bursts, generated in different half-cycles of the laser fields (as shown in the top part of figure 15(a)). However, only one of these bursts has a significant on-axis component, and the comparison of the radially integrated XUV time profiles before and after applying a 2 mrad spatial filter shows that one can beautifully isolate a single attosecond pulse with the help of phase matching (figure 15(c) and (a), respectively).

The phase matching driven isolation of a single attosecond pulse via spatial filtering can also be understood with the help of the phase matching maps shown in figure 3, from [63]. Although these phase matching maps are not generated for exactly the same conditions as the calculation shown in figure 15, they still illustrate the important features of the time gating mechanism. In figure 15, a spectral gate has already been applied which selects a range of harmonics from one of the lower half-cycle cutoffs, i.e. not the highest harmonic energies in the spectrum. As discussed above, these harmonics belong to the cutoff region during one half-cycle only, and to the upper plateau region for the half-cycles with higher peak electric fields. If we now look at the phase matching maps for a cutoff harmonic, shown in figure 3(e) and (f), we see that it is well phase matched on axis over several mm of propagation when the medium is placed 2 mm beyond the laser focus. In contrast, neither the short nor the long trajectory contribution to the upper plateau harmonics shown in figure 3(c)–(d) are phase matched on axis, but rather off axis and with diverging phase fronts. A spatial and spectral filter placed in the far field, selecting only the on-axis radiation around one of the lower half-cycle cutoffs, will therefore also temporally gate the XUV radiation to a single half-cycle's on-axis contribution, as in figure 15(a) and (b).

Experimental support for the idea of generating isolated attosecond pulses from individual half-cycle contributions to the harmonic radiation has been presented by Pfeifer and collaborators in [100]. They generated harmonics in neon by a 6 fs, 720 nm laser pulse and observed that a 15 eV wide region of the harmonic spectrum near the cutoff energy was quasi-continuous, supporting the bandwidth necessary for a single few-hundred attoseconds XUV pulse. Similarly to the work in [43], they interpreted the isolation mechanism in terms of different phase matching of different half-cycle contributions [101].

In contrast to the ionization driven spatio-temporal gating mechanism discussed in section 4.5, the phase matching driven mechanism discussed in this section does *not* depend on effects of ionization, which are minimal for the very low density used in the calculation in figure 15 [102]. The two gating mechanisms we have described (in this section and in 4.5) are therefore very different in nature and work in different regions of parameter space. The ionization gating through reshaping as presented in section 4.5 works in a loose-focusing and high-pressure regime and may lead to a larger XUV yield than the tight-focusing low-pressure phase matching gating approach in this section, simply because it allows one to have a larger and denser interaction volume. However, the phase matching gating described in this section takes advantage of near-perfect phase matching conditions for a range of harmonics during a particular time, which may make up for the difference in interaction volume. A combination of the two methods, employing phase matching gating in a situation where ionization is substantial and contributes both to spatio-temporal reshaping of the driving pulse and to the phase matching conditions, may be a very promising route to pursue.

4.7. Novel regime for phase matching: longer wavelength driving lasers

Technological developments over the past decade have made it possible to generate intense, few-cycle pulses at mid-infrared (MIR) wavelengths (between 1.5 μm and 4 μm, approximately) [46, 103–105], and there is an increasing interest in driving strong field processes with these sources [11, 27, 44, 45, 46, 48, 49]. The production of high harmonics and attosecond pulses is particularly interesting at MIR wavelengths since the ponderomotive energy and therefore the spectral cutoff is proportional to the wavelength squared. The same atom exposed to driving pulses with identical peak intensities would thus yield a cutoff energy four times larger with a 1.6 μm driving field than with an 800 nm driving field. The extended cutoff energy in MIR harmonic spectra has been experimentally demonstrated by several different groups [47, 45]. One can also expect to generate shorter attosecond pulses with MIR driving lasers, since the atto-chirp is inversely proportional to the wavelength [27]. For a detailed discussion of scaled interactions at longer wavelengths see [11, 27].

Tate and collaborators have recently investigated wavelength scaling laws of the yield and atto-chirp of harmonics, via numerical solutions of the SAE-TDSE using a pseudo potential for argon, and they show that the atto-chirp is indeed smaller at longer wavelength [27]. They also show that harmonics generated by MIR lasers have unexpectedly large contributions from electron trajectories longer than one optical cycle, i.e. trajectories much longer than what we have been referring to as the 'long' electron trajectory, compared with harmonics generated by 800 nm lasers [27]. It is interesting to note that this result is not reproduced by the strong field approximation which predicts that the two trajectories with returns within the first cycle to dominate the dipole response both at IR and MIR wavelengths. This may indicate an increased sensitivity to the effect of the atomic potential on the electron trajectories at MIR wavelengths, something which is ignored in the SFA.

The macroscopic aspects of few-cycle MIR driven generation of high-order harmonics and attosecond pulses have recently been addressed in calculations by Yakovlev and collaborators [44]. Their results present yet another example of how phase matching can form a time gate for the production of an isolated attosecond pulse, see figure 16. The top panel shows on-axis harmonic spectra in the far field generated by driving fields with different wavelengths after propagation

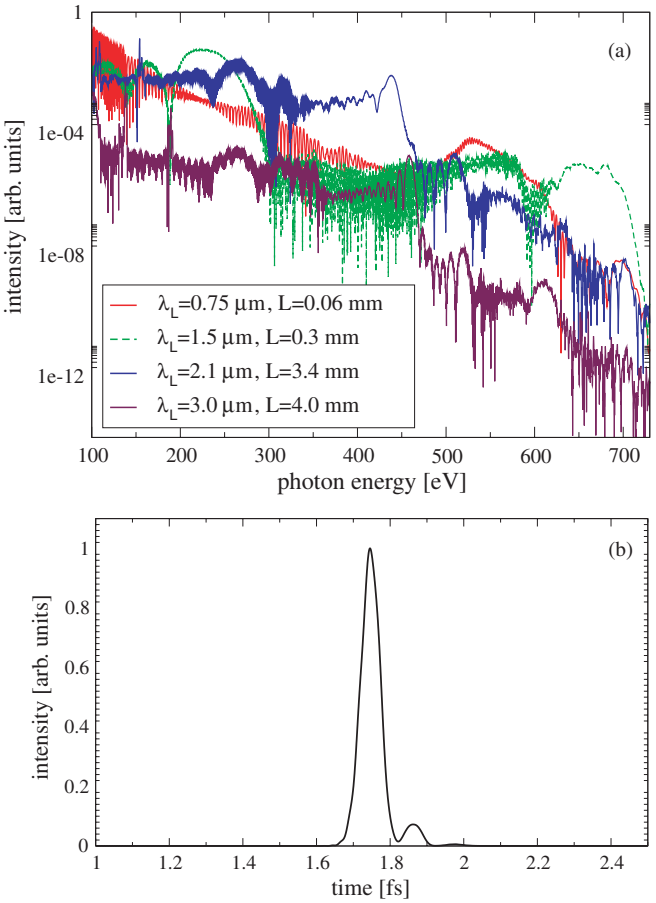

Figure 16. (a) On-axis, far-field harmonic spectra generated by MIR fields with different wavelengths, after propagation through a 100 mbar helium gas jet of varying length (see the text for details). (b) Time profile synthesized from the spectral range above 100 eV in the 1.5 μm spectrum. Reprinted with permission from [44]. Copyright (2007) by the Optical Society of America.

through a 100 mbar helium gas. Each driving pulse has a duration of two optical cycles and an initial peak intensity so as to give a cutoff energy of 700 eV. For the 1.5 μm driving pulse this corresponds to an initial intensity of approximately 10^{15} W cm^{-2}. The propagation lengths vary as each calculation has been terminated when the intensity has been reduced by 10% of its initial value.

The 1.5 μm spectrum in the top panel of figure 16 exhibits a 60 eV wide region in the lower plateau where the spectrum is continuous, indicating the presence of an isolated XUV burst. The time profile of these harmonics, after spectral gating with a filter that suppresses energies below 100 eV, is shown in the bottom panel of figure 16 and indeed presents an isolated pulse with a duration of only 60 as. Even though the driving pulse duration is only two optical cycles, the time-gating mechanism in this case is *not* the amplitude gating that leads to isolated attosecond pulses in the cutoff region of harmonics generated by few cycle pulses as discussed in section 4.2 above. Here, the time gating mechanism is due to phase matching and is similar to that proposed by Haworth and collaborators [43] in section 4.6, in that it relies on good phase matching for the long trajectory contribution to a specific range of harmonic radiation during one specific half-cycle of the driving pulse [106]. For MIR driving lasers, the dipole phase varies much more rapidly with intensity than at IR wavelengths since the action integral is given by $-\alpha U_p/\omega_1$ and therefore scales as $\lambda_1^3 I$. This means that the phase matching conditions are extremely sensitive to variation in the laser intensity along the propagation direction, even in loose focusing conditions, and that very good phase matching can be achieved only in very specific conditions. This allows for very efficient generation of a range of harmonics in one half-cycle and not in others. According to Yakovlev, the good phase matching of the long trajectory contribution leading to the single attosecond pulse in figure 16 is most likely due to a cancellation of the intensity-dependent dipole phase variation by the phase variation induced by the free electron dispersion [106].

The single-atom dipole moments used in the calculations by Yakovlev and collaborators were obtained using the strong field approximation, and for each XUV energy only including the shortest two quantum path contributions. The phase matching of longer quantum path contributions, found to be important in the work of Tate *et al* [27], remains to be investigated although one can speculate that it would be hard to find robust phase matching conditions for quantum path contributions with even steeper intensity-dependent phase variations.

4.8. Two-colour control of attosecond pulse generation

Adding a second field of different frequency and intensity to the intense IR field offers additional control over the generation of high-order harmonics and attosecond pulses. The presence of the second field breaks the half-cycle periodicity of the electron dynamics and offers an additional time gate compared to whatever other time gating mechanism is employed. The parameters that control the two-colour time gate are the relative frequencies, intensities and delay between the two fields. An important constraint for a two-colour control mechanism is that to be effective at a macroscopic level, all three of these parameters must remain more or less constant over the entire interaction volume.

Most two-colour control schemes relating to attosecond pulse generation involve a strong IR field and a weaker second harmonic field (which we will refer to as blue). Such a two-colour electric field has a periodicity of a full IR optical cycle, and the harmonic spectrum contains both odd and even harmonics. When the blue field is very weak it acts as a small phase perturbation to the one colour harmonic generation process, and by changing the relative delay one can control the intensity ratio between odd and even harmonics [87]. We will spend the rest of this section discussing the case where the second field is relatively strong, with an intensity of more than a few per cent of the IR intensity. In this case, the two-colour electric field in consecutive half-cycles is very different and the blue field substantially alters the electron continuum dynamics.

In a two-colour driving field, there are in general two different electric field 'evolutions' over one cycle of the IR field [50], see examples in figure 17(a). Each field evolution

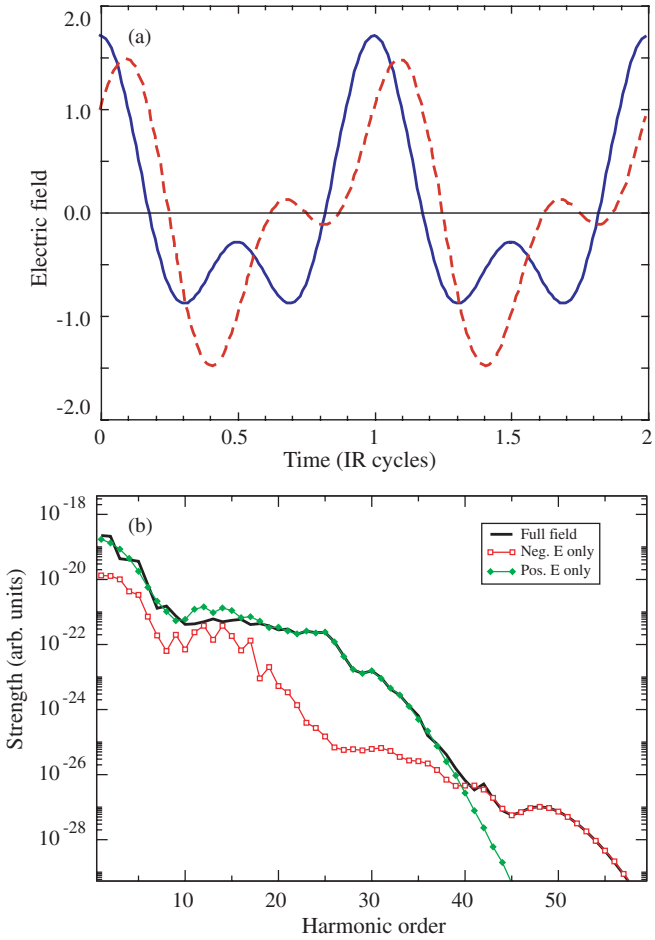

Figure 17. (a) Electric field time profile of IR-blue two-colour field where the blue intensity is half as strong as the red intensity, for two different delays. The electric field is given in units of the IR alone electric field strength. (b) Harmonic spectra generated in argon by the electric field shown with solid line in (a). We have separately calculated the contribution from the two electric field evaluations, see [50] for details.

gives rise to its own family of trajectories which can be strongly perturbed compared to the one-colour trajectories. For most delays, one evolution has first a strong half-cycle, followed by a much weaker half-cycle. This evolution in general gives electron trajectories that are released at a relatively strong electric field, and are pushed back to the core by a relatively weak electric field. The harmonic spectrum generated by these trajectories has a high yield and a low cutoff energy. The other electric field evolution starts with a weak half-cycle and is followed by a strong half-cycle, and gives rise to a harmonic spectrum with a low yield but a much higher cutoff energy. In [50], Mauritsson *et al* showed that the two spectra can often be observed separately in a calculated harmonic spectrum, as shown in figure 17(b).

For the particular delay used in figure 17(b), the spectra from the two families of trajectories each represent radiation which is emitted only once per IR cycle. The time structure of a selection of harmonics close to either of the two cutoffs in the full spectrum will therefore exhibit only one attosecond XUV burst per IR cycle. This means that it is in principle possible to produce isolated attosecond pulses with a driving pulse that is twice as long as in the IR alone case, or attosecond pulse trains with only one attosecond burst per full cycle of the IR field. Attosecond pulse trains generated around the low-energy, high-yield cutoff were produced experimentally by Mauritsson *et al* [50]. In an experiment by Oishi and collaborators, a supercontinuous harmonic spectrum was produced in argon using a 9 fs, two-colour driving field, indicating the presence of an isolated attosecond pulse [52]. The production of isolated attosecond pulses from a three to four cycle driving pulse employing two-colour control has been shown in single-atom calculations by several different groups [51, 107, 108]. Chang and collaborators have recently proposed using two-colour control in combination with polarization gating to form a so-called double optical gate [109, 110]. Their experimentally produced supercontinuum supports an isolated attosecond pulse with a duration of 130 as [110].

In all of these scenarios, the extra time-gating mechanism compared to IR-driven attosecond pulse generation is provided by the blue field which for certain delays suppresses every other attosecond burst. In order for this approach to be successful at a macroscopic level it is, as we said, necessary to keep the delay and the relative intensities close to constant over the entire interaction volume. It is by definition impossible to keep the intensity ratio and relative delay exactly constant over the entire interaction region, because of the different diffraction properties of fields of different wavelengths. For a Gaussian beam, the confocal parameter b is related to its waist w_f in the focus by $b = 2\pi w_f^2/\lambda$. The confocal parameter controls the evolution of the intensity and phase of the beam along the axis of propagation, and the waist controls the evolution in the radial direction. In general, one has to choose whether to match the axial or the radial dependence of the two beams. We find that it is better for two-colour attosecond pulse control to match the radial than the axial dependence of the beams (see for instance [111]). This is because the confocal parameters of both beams are in general much longer than the nonlinear medium (typically 1–2 cm compared with 1–2 mm), and the relative change in intensity and phase over the length of the medium can be kept small even if the confocal parameters differ by a factor of 2. In contrast, if the waists of the two beams are substantially different then it is only in part of the interaction volume that one actually exerts two-colour control over the generation process, and there will likely be a substantial contribution to the harmonic signal from the remaining volume. This is particularly a problem if the weak control field is smaller than the IR field so that there is substantial IR-alone harmonics generated off axis, and is less severe if the weak control field is the larger of the two beams. We note here that matching the focused waists of two beams with different wavelengths requires either using two different focusing elements or increasing the (unfocused) size of one beam with respect to the other.

Another issue for two-colour control is ionization-induced defocusing and de-phasing which affects long wavelength fields more than short wavelength fields because the plasma contribution to the refractive index is proportional to the wavelength squared. A particularly difficult case in this respect is two-colour control using a *sub-harmonic* of the IR laser as

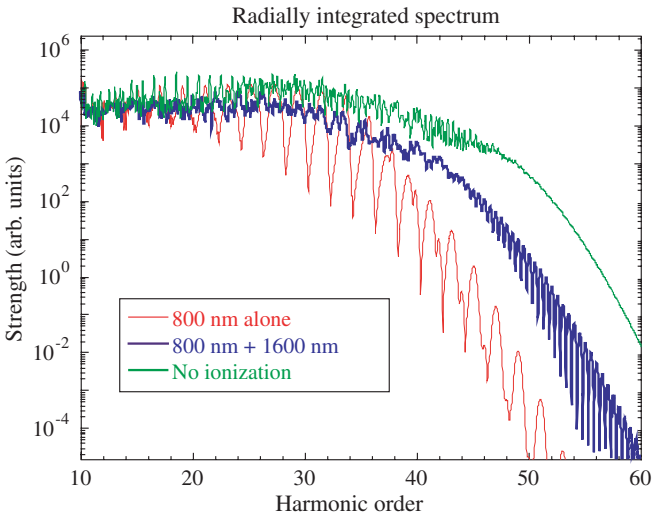

Figure 18. Harmonic spectra after propagation through short (1 mm), low-pressure (30 Torr) argon gas medium, generated by an IR-MIR two-colour field (see the text for details).

the second field. A two-colour field consisting of a strong 800 nm field and a weaker 1600 nm field has a periodicity of two IR optical cycles. Pfeifer and collaborators showed in single-atom calculations that because of this extended periodicity, it is possible to generate an isolated attosecond burst with a 24 fs driving pulse by selecting only harmonics above the IR cutoff energy, for certain delays between the two fields [112].

In the following, we investigate the effects of ionization-induced defocusing driven by a $\omega_1, \omega_1/2$ two-colour field. We calculate the macroscopic response of a 1 mm long argon gas jet with a density of 10^{18} atoms cm^{-3} (corresponding to a pressure of about 30 Torr) to an intense two-colour driving pulse with a duration of 24 fs. The peak intensity of the 810 nm IR pulse is 2.25×10^{14} W cm^{-2} and that of the 1620 nm MIR pulse is 2.25×10^{12} W cm^{-2}. The relative delay between the two pulses has been chosen so as to optimize the generation of an isolated attosecond pulse (see below) and is $-0.7T_1$. This differs from the single-atom optimum delay of zero because of propagation effects. The confocal parameters are 2 cm and 4 cm for the MIR and the IR beams, respectively, which means that they have the same waists in their common focus. The radially integrated harmonic spectrum at the end of the argon gas is shown in figure 18.

For comparison, in figure 18 we also show the spectrum generated by the IR field alone. It is the two-colour XUV radiation generated at frequencies beyond the IR-alone cutoff energy that can reasonably be expected to comprise an isolated attosecond pulse after spectral filtering, i.e. radiation above approximately $40\omega_1$. The top-most spectrum in figure 18 shows the two-colour spectrum one would get in the absence of the ionization-induced free electron contribution to the refractive index. Two consequences of ionization can be seen in the comparison of the spectra: (i) ionization-induced defocusing decreases the peak intensity which reduces the cutoff energy and (ii) the no-ionization spectrum is much less modulated at high energy, indicating that the time structure of the radiation beyond $40\omega_1$ is more likely to be emitted in a single burst. We note that the no-ionization spectrum has been calculated for a relative delay of zero which was the optimal delay for producing isolated attosecond pulses in the single-atom calculations.

Figure 19 illustrates the effect of ionization-induced defocusing and dephasing on the two-colour field. We show the spatio-spectral profiles of the IR and MIR beams separately at the beginning and at the end of the argon gas. It is clear that the MIR beam is affected much more by ionization. As a result of the spatial variation of the plasma refractive index, the radial profile is much flatter for the MIR beam than for the IR beam, and the reduction of the on-axis intensity is much larger. As a result of the temporal variation of the plasma

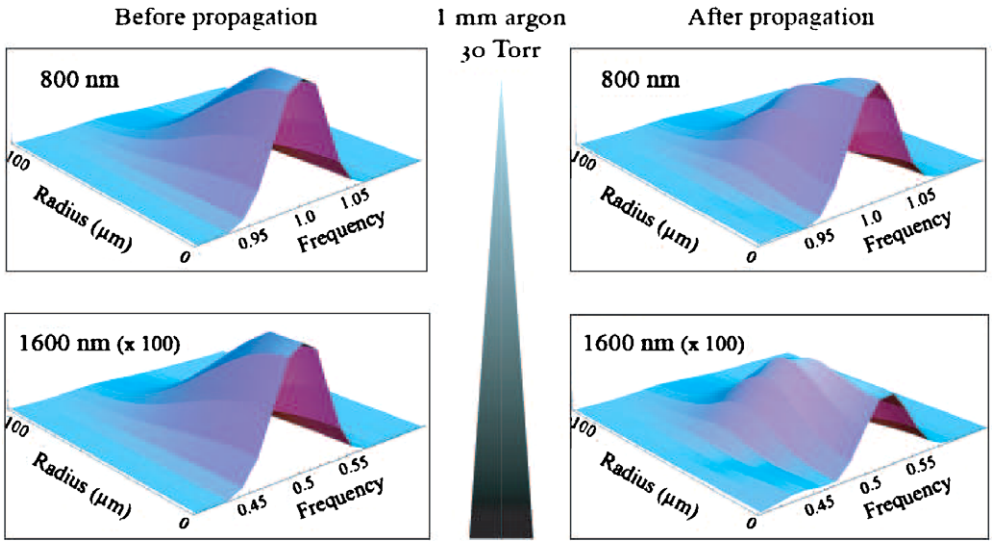

Figure 19. Spatio-spectral profiles of the IR and the MIR field at the beginning and at the end of the argon jet. The IR field is essentially unchanged after propagation through the short medium, but the MIR field is strongly altered by effects of ionization, both spatially (has been defocused), and spectrally (blue-shifted).

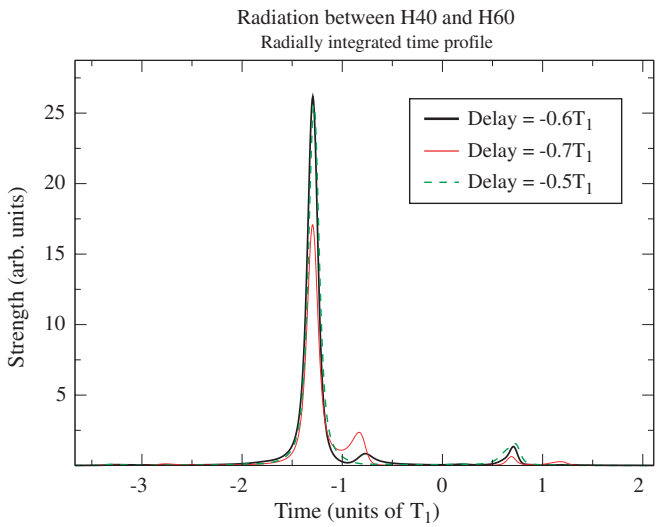

Figure 20. Time profile of XUV radiation between harmonics 40 and 60, generated by the two-colour IR-MIR field discussed in the text. We show the time profile generated at three different relative delays between the IR and the MIR field, showing that the attosecond isolation process is relatively robust with respect to small changes in the delay.

refractive index, the on-axis blue shift of the MIR frequency is larger than that of the IR frequency. Furthermore, the MIR beam exhibits a more complicated spatio-spectral shape where the central frequency changes with r. The dual effects of ionization are thus to reduce the spatial overlap between the two beams, and to cause a temporal phase shift which varies with r. Phrased in terms of the two-colour control parameters, ionization causes both the relative intensities and phases to change with propagation distance.

In spite of the dephasing caused by ionization in this two-colour scheme, phase matching can still allow the generation of an isolated attosecond pulse. The time profile of harmonics 40–60 from the propagated spectrum is shown in figure 20. The limitation of phase matching and ionization in this case is that the yield (which is quite low for argon, 0.1 pJ at 50 eV) does not scale up well. Increasing either the intensity or the pressure will increase the effects of ionization. This means that not only does the yield not scale up with intensity and pressure, but that eventually it will no longer be possible to isolate a single attosecond pulse due to the de-phasing effects. The only way to increase the yield is by brute-force scaling of interaction volume: increasing both confocal parameters proportionately which requires a higher laser energy.

5. Main challenge for attosecond sources—enhancement of yield and control of coherence properties

In this review, we have outlined how macroscopic effects often play a crucial role in the generation of attosecond pulses in a number of different scenarios, forming temporal or spatial gates for isolating only the useful part of the XUV radiation. Macroscopic effects are of course also extremely important in the more traditional sense of determining the yield and the coherence properties of the attosecond pulses. Improving the yield of attosecond pulses while maintaining control of their spatial and temporal coherence properties will likely remain a challenge for attosecond source development into the next decade, as it requires the control of tens or hundreds of eV of bandwidth deep in the XUV spectral region.

While only a few studies have explicitly addressed optimization of attosecond pulse generation [113–115], there have been a range of studies on how to improve the yield and coherence properties of high-order harmonics via phase matching. In the following we mention a few of these studies, many of which could be extended directly to the optimization of attosecond pulses.

Several groups have explored optimal control approaches, where optimization of some property of the harmonic radiation is achieved via a feedback loop that is coupled to a pulse-shaper, in most cases optimizing the yield of particular harmonics [113, 114, 116–118]. For a recent review of using optimal control methods to optimize harmonic generation, which also discusses spatial shaping of the driving beam, and optimizing properties other than the yield, see [118]. A few theoretical studies have optimized the generation of attosecond pulses directly, either through temporal pulse shaping [114] or choice of focusing conditions [113].

Many groups have used quasi-phase matching to improve the yield of high-order harmonics [18, 31, 65, 66, 115, 119, 120, 121]. The basic premise of quasi-phase matching is to dramatically improve yield in a medium which is much longer than the coherence length, by having the gas density be zero during the part of the propagation where new radiation interferes destructively with the already propagating radiation, allowing only constructive build-up of the radiation. The Murnane/Kapteyn group has successfully employed more general approaches to quasi-phase matching using modulated wave guides and counter-propagating light, in both cases modulating the generating light rather than the generating material [18, 65, 66, 119, 120]. In a very recent study, Tosa and collaborators optimize the yield of MIR driven isolated attosecond pulses via quasi-phase matching in a series of thin gas jets placed one after the other [115].

In a range of other experimental and theoretical studies, the yield of harmonics has been optimized through changing the length and pressure of the nonlinear medium [122, 123], the spatial structure of the laser beam [69, 124–128], or by using ions in a capillary discharge to improve yield of very high-order harmonics [129]. Taking advantage of the combined effects of ionization-induced defocusing and Kerr effect self-focusing in a very long medium at high intensity [130], and using a mixture of argon and helium gases to improve phase matching conditions in a long medium [131, 132] have also been studied.

A novel source of very high-order harmonics which shows promise for increasing the yield of attosecond pulses by several orders of magnitude, compared to gas phase harmonic generation as described in this review, is the interaction between a relativistically intense laser pulse and an overdense plasma created at the surface of a solid by the laser pulse. Although the temporal structure of the generated XUV

radiation still remains to be characterized experimentally, very high photon energies have been observed in both experiments and calculations with very high conversion efficiencies [133–136].

6. Summary

We have reviewed the macroscopic aspects of attosecond pulse production in a number of different generation schemes. We have discussed how in each case the attosecond pulses are *selected* from among a complex spectral and spatial distribution of XUV radiation. We have shown that macroscopic effects such as phase matching and ionization always play a role in this selection process, in most cases enabling the formation of the attosecond pulses and in a few cases limiting it.

The progress of attosecond science will be closely connected with the improvement of attosecond sources in terms of their yield and coherence properties. Exploiting nonlinearities at the macroscopic level, in addition to novel single-atom generation and control schemes, is a promising route to shorter and more intense attosecond pulses.

Acknowledgments

We are very grateful to C Altucci, A L'Huillier, T Pfeifer, J Tisch and V Yakovlev for discussing their work with us. This material is based upon work supported by the National Science Foundation through grant nos PHY-0449235 and PHY-0701372, and through the Center for Computation and Technology at Louisiana State University.

References

[1] Hentschel M, Kienberger R, Spielmann C, Reider G A, Milosevic N, Brabec T, Corkum P, Heinzmann U, Drescher M and Krausz F 2001 *Nature* **414** 509
[2] Paul P M, Toma E S, Breger P, Mullot G, Augé F, Balcou P, Muller H G and Agostini P 2001 *Science* **292** 1689
[3] Drescher M, Hentschel M, Kienberger R, Uiberacker M, Yakovlev V, Scrinzi A, Westerwalbesloh T, Kleineberg U, Heinzmann U and Krausz F 2002 *Nature* **419** 803
[4] Kienberger R *et al* 2004 *Nature* **427** 817
[5] Goulielmakis E *et al* 2004 *Science* **305** 1267
[6] Johnsson P *et al* 2005 *Phys. Rev. Lett.* **95** 013001
[7] Fohlisch A, Feulner P, Hennies F, Fink A, Menzel D, Sanchez-Portal D, Echenique P M and Wurth W 2005 *Nature* **436** 373
[8] Uiberacker M *et al* 2007 *Nature* **446** 627
[9] Cavalieri A L *et al* 2007 *Nature* **449** 1029
[10] Mauritsson J, Johnsson P, Gustafsson E, Swoboda M, Ruchon T, L'Huillier A and Schafer K J 2008 *Phys. Rev. Lett.* **100** 073003
[11] Agostini P and DiMauro L F 2004 *Rep. Prog. Phys.* **67** 813
[12] Corkum P B and Krausz F 2007 *Nature Phys.* **3** 381
[13] Kulander K C, Schafer K J and Krause J L 1993 *Super Intense Laser Atom Physics* ed B Pireaux, A L'Huillier and J Rzazewski (New York: Plenum)
[14] Ferray M, L'Huillier A, Li X F, Lomreé L A, Mainfray G and Manus C 1988 *J. Phys. B: At. Mol. Opt. Phys.* **21** L31
[15] Wahlström C G, Larsson J, Persson A, Starczewski T, Svanberg S, Salières P, Balcou P and L'Huillier A 1993 *Phys. Rev.* A **48** 4709
[16] Krause J L, Schafer K J and Kulander K C 1992 *Phys. Rev. Lett.* **68** 3535
[17] Chang Z, Rundquist A, Wang H, Murnane M M and Kapteyn H C 2001 *Phys. Rev. Lett.* **79** 2967
[18] Gibson E A *et al* 2003 *Science* **302** 95
[19] Seres E, Seres J and Spielmann C 2006 *Appl. Phys. Lett.* **89** 181919
[20] Schafer K J and Kulander K C 1997 *Phys. Rev. Lett* **78** 638
[21] Lewenstein M, Balcou P, Ivanov M Y, L'Huillier A and Corkum P B 1994 *Phys. Rev.* A **49** 2117
[22] Schafer K J, Yang B, DiMauro L F and Kulander K C 1993 *Phys. Rev. Lett.* **70** 1599
[23] Corkum P B 1993 *Phys. Rev. Lett.* **71** 1994
[24] Lewenstein M, Salières P and L'Huillier A 1995 *Phys. Rev.* A **52** 4747
[25] Salières P *et al* 2001 *Science* **292** 902
[26] Antoine P, L'Huillier A and Lewenstein M 1996 *Phys. Rev. Lett.* **77** 1234
[27] Tate J, Auguste T, Muller H G, Salières P, Agostini P and DiMauro L F 2007 *Phys. Rev. Lett.* **98** 013901
[28] Christov I P 1999 *Opt. Lett.* **24** 1425
[29] Bohan A de, Antoine P, Milosevic D B and Piraux B 1998 *Phys. Rev. Lett.* **81** 1837
[30] Milosevic N, Scrinzi A and Brabec T 2002 *Phys. Rev. Lett.* **88** 093905
[31] Seres J, Yakovlev V S, Seres E, Streli C, Wobrauschek P, Spielmann C and Krausz F 2007 *Nature Phys.* **3** 878
[32] Seres J, Seres E, Verhoef A J, Tempea G, Streli C, Wobrauschek P, Yakovlev V, Scrinzi A, Spielmann C and Krausz F 2005 *Nature* **433** 596
[33] Sola I J *et al* 2006 *Nature Phys.* **2** 319
[34] Sansone G *et al* 2006 *Science* **314** 443
[35] Corkum P B, Burnett N H and Ivanov M Y 1994 *Opt. Lett.* **19** 1870
[36] Antoine P, L'Huillier A, Lewenstein M, Salières P and Carré B 1996 *Phys. Rev.* A **53** 1725
[37] Antoine P, Milosević D B, L'Huillier A, Gaarde M B, Salières P and Lewenstein M 1997 *Phys. Rev.* A **56** 4960
[38] Chang Z 2004 *Phys. Rev.* A **70** 043802
[39] Chang Z 2005 *Phys. Rev.* A **71** 023813
[40] He F, Ruiz C and Becker A 2007 *Opt. Lett.* **32** 3224
[41] Altucci C, Tosa V and Velotta R 2007 *Phys. Rev.* A **75** 061401R
[42] Gaarde M B and Schafer K J 2006 *Opt. Lett.* **31** 3188
[43] Haworth C A, Chipperfield L E, Robinson J S, Knight P L, Marangos J P and Tisch J W G 2007 *Nature Phys.* **3** 52
[44] Yakovlev V S, Ivanov M and Krausz F 2007 *Opt. Exp.* **15** 15351
[45] Colosimo P *et al* 2008 *Nat. Phys.* **4** 386
[46] Sheehy B, Martin J D D, DiMauro L F, Agostini P, Schafer K J, Gaarde M B and Kulander K C 1999 *Phys. Rev. Lett.* **83** 5270
[47] Shan B and Chang Z 2001 *Phys. Rev.* A **65** 011804
[48] Gordon A and Kärtner F 2005 *Opt. Exp.* **13** 2941
[49] Frolov M V, Manakov N L and Starace A F 2008 *Phys. Rev. Lett.* **100** 173001
[50] Mauritsson J, Johnsson P, Gustafsson E, L'Huillier A, Schafer K J and Gaarde M B 2006 *Phys. Rev. Lett.* **97** 013001
[51] Pfeifer T, Gallmann L, Abel M J, Neumark D M and Leone S R 2006 *Opt. Lett.* **31** 975
[52] Oishi Y, Kaku M, Suda A, Kannari F and Midorikawa K 2006 *Opt. Exp.* **14** 7230
[53] Salières P, L'Huillier A and Lewenstein M 1995 *Phys. Rev. Lett.* **74** 3776
[54] L'Huillier A *et al* 1995 *J. Nonlinear Opt. Phys. Mater.* **4** 647
[55] Balcou P, Salières P, L'Huillier A and Lewenstein M 1997 *Phys. Rev.* A **55** 3204

[56] Milonni P W and Eberly J H 1988 *Lasers* (New York: Wiley)
[57] Bellini M, Lyngå C, Tozzi A, Gaarde M B, Hänsch T W, L'Huillier A and Wahlström C G 1998 *Phys. Rev. Lett.* **81** 297
[58] Salieres P, Antoine P, Bohan A de and Lewenstein M 1998 *Phys. Rev. Lett.* **81** 5544
[59] Gaarde M B, Salin F, Constant E, Balcou P, Schafer K J, Kulander K C and L'Huillier A 1999 *Phys. Rev.* A **59** 1367
[60] Murakami M, Mauritsson J and Gaarde M B 2005 *Phys. Rev.* A **72** 023413
[61] Mairesse Y *et al* 2003 *Science* **302** 1540
[62] Varjú K *et al* 2005 *J. Mod. Opt.* **52** 379
[63] Chipperfield L, Knight P, Tisch J and Marangos J 2006 *Opt. Commun.* **264** 494
[64] Tempea G, Geissler M, Schnürer M and Brabec T 2000 *Phys. Rev. Lett.* **84** 4329
[65] Christov I, Kapteyn H and Murnane M 2000 *Opt. Exp.* **7** 362
[66] Paul A, Bartels R A, Tobey R, Green H, Weiman S, Christov I P, Murnane M M, Kapteyn H C and Backus S 2003 *Nature* **421** 51
[67] Ruchon T, Hauri C P, Varjú K, Mansten E, Swoboda M, López-Martens R and L'Huillier A 2008 *New J. Phys.* **10** 025027
[68] Constant E, Garzella D, Breger P, Mével E, Dorrer C, Blanc C L, Salin F and Agostini P 1999 *Phys. Rev. Lett.* **82** 1668
[69] Hergott J F, Kovacev M, Merdji H, Hubert C, Mairesse Y, Jean E, Breger P, Agostini P, Carré B and Salières P 2002 *Phys. Rev.* A **66** 021801
[70] Rae S C, Burnett K and Cooper J 1994 *Phys. Rev.* A **50** 3438
[71] Gaarde M B, Murakami M and Kienberger R 2006 *Phys. Rev.* A **74** 053401
[72] Geissler M, Tempea G and Brabec T 2000 *Phys. Rev.* A **62** 033817
[73] Brabec T and Krausz F 2000 *Rev. Mod. Phys.* **72** 545
[74] Lorin E, Chelkowski S and Bandrauk A D 2007 *Comput. Phys. Commun.* **177** 908
[75] Priori E *et al* 2000 *Phys. Rev.* A **61** 063801
[76] Shon N H, Suda A and Midorikawa K 2000 *Phys. Rev.* A **62** 023801
[77] Henke B, Gullikson E and Davis J 1993 *At. Data Nucl. Data Tables* **54** 181
[78] L'Huillier A, Li X F and Lompré L A 1990 *J. Opt. Soc. Am.* B **7** 527
[79] Rae S C and Burnett K 1992 *Phys. Rev.* A **46** 1084
[80] Ammosov M V, Delone N B and Krainov V P 1986 *Sov. Phys.—JETP* **64** 1191
[81] Murakami M 2006 High harmonic generation by short laser pulses: time-frequency behavior and applications to attophysics *Dissertation* Louisiana State University (unpublished)
[82] Perelomov A M, Popov V S and Terentev M V 1966 *Sov. Phys.—JETP* **23** 924
[83] Larochelle S F J, Talebpour A and Chin S L 1998 *J. Phys. B: At. Mol. Opt. Phys.* **31** 1215
[84] Krainov V P 1997 *J. Opt. Soc. Am.* B **14** 425
[85] Becker A, Plaja L, Moreno P, Nurhuda M and Faisal F H M 2001 *Phys. Rev.* A **64** 023408
[86] Vanne Y V and Saenz A 2007 *Phys. Rev.* A **75** 063403
[87] Dudovich N, Smirnova O, Levesque J, Mairesse Y, Ivanov M Y, Villeneuve D M and Corkum P B 2006 *Nature Phys.* **2** 781
[88] Gaarde M B and Schafer K J 2002 *Phys. Rev.* A **65** 031406
[89] Kulander K C, Schafer K J and Krause J L 1992 *Atoms in Intense Laser Fields* ed M Gavrila (San Diego, CA: Academic) pp 247–300
[90] Balcou P, Dederichs A S, Gaarde M B and L'Huillier A 1999 *J. Phys. B: At. Mol. Opt. Phys.* **32** 2973
[91] L'Huillier A, Balcou P, Candel S, Schafer K J and Kulander K C 1992 *Phys. Rev.* A **46** 2778
[92] Lorin E, Chelkowski S and Bandrauk A D 2008 *New J. Phys.* **10** 025033
[93] Lyngå C, Gaarde M B, Delfin C, Bellini M, Hänsch T W, L'Huillier A and Wahlström C G 1999 *Phys. Rev.* A **60** 4823
[94] López-Martens R *et al* 2005 *Phys. Rev. Lett.* **94** 033001
[95] Nisoli M, Silvestri S D, Svelto O, Szipöcz R, Ferencz K, Spielmann C, Sartania S and Krausz F 1997 *Opt. Lett.* **22** 522
[96] Hauri C P, Kornelis W, Helbing F W, Heinrich A, Couairon A, Mysyrowicz A, Biegert J and Keller U 2004 *Appl. Phys.* B **79** 673
[97] Stibenz G, Zhavoronkov N and Steinmeyer G 2006 *Opt. Lett.* **31** 274
[98] Chakraborty H S, Gaarde M B and Couairon A 2006 *Opt. Lett.* **31** 3662
[99] Budil K S, Salières P, L'Huillier A, Ditmire T and Perry M D 1993 *Phys. Rev.* A **48** 3437R
[100] Pfeifer T, Jullien A, Abel M J, Nagel P M, Gallmann L, Neumark D M and Leone S R 2007 *Optics Exp.* **15** 17120
[101] Pfeifer T 2008 private communication
[102] Tisch J W G 2008 private communication
[103] Fuji T, Ishii N, Teisset C Y, Gu X, Metzger T and Baltuŝka A 2006 *Opt. Lett.* **31** 1103
[104] Vozzi C *et al* 2006 *Opt. Exp.* **14** 10109
[105] Hauri C P *et al* 2007 *Opt. Lett.* **32** 868
[106] Yakovlev V 2008 private communication
[107] Cao W, Lu P, Lan P, Wang X and Yang G 2007 *Opt. Exp.* **15** 530
[108] Zeng Z, Cheng Y, Song X, Li R and Xu Z 2007 *Phys. Rev. Lett.* **98** 203901
[109] Chang Z 2007 *Phys. Rev.* A **76** 051403R
[110] Gilbertson S, Mashiko H, Li C, Khan S D, Shakya M M, Moon E and Chang Z 2008 *Appl. Phys. Lett.* **92** 071109
[111] Gaarde M B, Schafer K J, Heinrich A, Biegert J and Keller U 2005 *Phys. Rev.* A **72** 013411
[112] Pfeifer T, Gallmann L, Abel M J, Nagel P M, Neumark D M and Leone S R 2006 *Phys. Rev. Lett.* **97** 163901
[113] Roos L, Gaarde M B and L'Huillier A 2001 *J. Phys. B: At. Mol. Opt. Phys.* **34** 5041
[114] Xiao J, Sun Z, Zhang X, Wang Y, Zhang W, Wang Z, Li R and Xu Z 2006 *J. Opt. Soc. Am.* B **23** 771
[115] Tosa V, Yakovlev V S and Krausz F 2008 *New J. Phys.* **10** 025016
[116] Bartels R S, Zeek E, Misogutti L, Vdovin G, Christov I P, Murnane M M and Kapteyn H C 2000 *Nature* **406** 164
[117] Boyko O, Valentin C, Mercier B, Coquelet C, Pascal V, Papalazarou E, Rey G and Balcou P 2007 *Phys. Rev.* A **76** 063811
[118] Winterfeldt C, Spielmann C and Gerber G 2008 *Rev. Mod. Phys.* **80** 117
[119] Cohen O, Zhang X, Lytle A L, Popmintchev T, Murnane M M and Kapteyn H C 2007 *Phys. Rev. Lett.* **99** 053902
[120] Zhang X, Lytle A L, Popmintchev T, Zhou X, Kapteyn H C, Murnane M M and Cohen O 2007 *Nature Phys.* **3** 270
[121] Landreman M, O'Keeffe K, Robinson T, Zepf M, Dromey B and Hooker S M 2007 *J. Opt. Soc. Am.* B **24** 2421
[122] Delfin C, Lisio C de, Altucci C, Filippo F D, Gaarde M B, L'Huillier A and Wahlström C G 1999 *J. Phys. B: At. Mol. Opt. Phys.* **32** 5397
[123] Altucci C, Starczewski T, Mevel E, Wahlström C-G, Carré B and L'Huillier A 1996 *JOSA* B **13** 148
[124] Roos L, Constant E, Mevel E, Balcou P, Déscamps D, Gaarde M B, L'Huillier A, Valette A and Haroutunian R 1999 *Phys. Rev.* A **60** 5010
[125] Takahashi E, Nabekawa Y and Midorikawa K 2002 *Opt. Lett.* **27** 1920

[126] Nisoli M *et al* 2002 *Phys. Rev. Lett* **88** 033902
[127] Altucci C *et al* 2003 *Phys. Rev.* A **68** 033806
[128] Tosa V, Takahashi E, Nabekawa Y and Midorikawa K 2003 *Phys. Rev.* A **67** 063817
[129] Reagan B A, Popmintchev T, Grisham M E, Gaudiosi D M, Berrill M, Cohen O, Walker B C, Murnane M M, Rocca J J and Kapteyn H C 2007 *Phys. Rev.* A **76** 013816
[130] Painter J C, Adams M, Brimhall N, Christensen E, Giraud G, Powers N, Turner M, Ware M and Peatross J 2006 *Opt. Lett.* **31** 3471
[131] Kanai T, Takahashi E J, Nabekawa Y and Midorikawa K 2007 *Phys. Rev. Lett.* **98** 153904
[132] Takahashi E J, Kanai T, Ishikawa K L, Nabekawa Y and Midorikawa K 2007 *Phys. Rev. Lett.* **99** 053904
[133] Gordienko S, Pukhov A, Shorokhov O and Baeva T 2004 *Phys. Rev. Lett.* **93** 115002
[134] Dromey B *et al* 2006 *Nature Phys.* **456** 2
[135] Tsakiris G D, Eidmann K, Meyer-ter-Vehn J and Krausz F 2006 *New J. Phys.* **8** 19
[136] Thaury C *et al* 2007 *Nature Phys.* **3** 424